Relating geostationary satellite measurements of aerosol optical depth (AOD) over East Asia to fine particulate matter (PM$_{2.5}$): insights from the KORUS-AQ aircraft campaign and GEOS-Chem model simulations

Shixian Zhai[1], Daniel J. Jacob[1], Jared F. Brewer[1], Ke Li[1], Jonathan M. Moch[1], Jhoon Kim[2,3], Seoyoung Lee[2], Hyunkwang Lim[2], Hyun Chul Lee[3], Su Keun Kuk[3], Rokjin J. Park[4], Jaein I. Jeong[4], Xuan Wang[5], Pengfei Liu[6], Gan Luo[7], Fangqun Yu[7], Jun Meng[8], Randall V. Martin[9], Katherine R. Travis[10], Johnathan W. Hair[10], Bruce E. Anderson[10], Jack E. Dibb[11], Jose L. Jimenez[12], Pedro Campuzano-Jost[12], Benjamin A. Nault[12,a], Jung-Hun Woo[13], Younha Kim[14], Qiang Zhang[15], Hong Liao[16]

[1]Harvard John A. Paulson School of Engineering and Applied Sciences, Harvard University, Cambridge, MA, USA

[2]Department of Atmospheric Sciences, Yonsei University, Seoul, Republic of Korea

[3]Samsung Particulate Matter Research Institute, Samsung Advanced Institute of Technology, 130 Samsung-ro, Yeongtong-gu, Suwon-si, Gyeonggi-do, Republic of Korea

[4]School of Earth and Environmental Sciences, Seoul National University, Seoul, Republic of Korea

[5]School of Energy and Environment, City University of Hong Kong, Hong Kong SAR, China

[6]School of Earth and Atmospheric Sciences, Georgia Institute of Technology, Atlanta, GA, USA

[7]Atmospheric Sciences Research Center, University at Albany, Albany, New York, USA

[8]Department of Atmospheric & Oceanic Sciences, University of California, Los Angeles, California, USA

[9]Department of Energy, Environmental & Chemical Engineering, Washington University in St Louis, MO, USA

[10]NASA Langley Research Center, Hampton, VA, USA

[11]Institute for the Study of Earth, Oceans, and Space, University of New Hampshire, Durham, NH, USA

[12]Department of Chemistry, and Cooperative Institute for Research in Environmental Sciences, University of Colorado, Boulder, CO, USA

[13]Department of Civil and Environmental Engineering, Konkuk University, Seoul, Republic of Korea

[14]International Institute for Applied Systems Analysis (IIASA), 2361 Laxenburg, Austria

[15]Department of Earth System Science, Tsinghua University, Beijing, China.

[16]Jiangsu Key Laboratory of Atmospheric Environment Monitoring and Pollution Control, Collaborative Innovation Center of Atmospheric Environment and Equipment Technology, School of Environmental Science and Engineering, Nanjing University of Information Science and Technology, Nanjing, China.

[a] Now at Center for Aerosol and Cloud Chemistry, Aerodyne Research, Inc., Billerica, MA, USA

Correspondence: Shixian Zhai (zhaisx@g.harvard.edu)

Abstract. Geostatistics satellite measurements of aerosol optical depth (AOD) over East Asia from the GOCI and AHI instruments can augment surface monitoring of fine particulate matter (PM$_{2.5}$) air quality, but this requires better understanding of the AOD-PM$_{2.5}$ relationship. Here we use the GEOS-Chem chemical transport model to analyze the critical variables determining the AOD-PM$_{2.5}$ relationship over East Asia by simulation of observations from satellite, aircraft, and ground-based datasets. This includes the detailed vertical aerosol profiling over South Korea from the KORUS-AQ aircraft campaign (May-June 2016) with concurrent ground-based PM$_{2.5}$ composition, PM$_{10}$, and AERONET AOD measurements. The KORUS-AQ data show that 550 nm AOD is mainly contributed by sulfate-nitrate-ammonium (SNA) and organic aerosols in the planetary boundary layer (PBL), despite large dust concentrations in the free troposphere, reflecting the optically effective size and high hygroscopicity of the PBL aerosols. We updated SNA and organic aerosol size distributions in GEOS-Chem to represent aerosol optical properties over East Asia by using in-situ measurements of particle size distributions from KORUS-AQ. We find that SNA and organic aerosols over East Asia have larger size (number median radius of 0.11 µm with geometric standard deviation of 1.4) and 20% larger mass extinction efficiency as compared to aerosols over North America (default setting in GEOS-Chem). Although GEOS-Chem is successful in reproducing the KORUS-AQ vertical profiles of aerosol mass, its ability to link AOD to PM$_{2.5}$ is limited by under-accounting of coarse PM and by a large overestimate of nighttime PM$_{2.5}$ nitrate. The GOCI/AHI AOD data over East Asia in different seasons show agreement with AERONET AODs and a spatial distribution consistent with surface PM$_{2.5}$ network data. The AOD observations over North China show a summer maximum and winter minimum, opposite in phase to surface PM$_{2.5}$. This is due to low PBL depths compounded by high residential coal emissions in winter, and high relative humidity (RH) in summer. Seasonality of AOD and PM$_{2.5}$ over South Korea is much weaker, reflecting weaker variation of PBL depth and lack of residential coal emissions.

1   Introduction

PM$_{2.5}$ (particulate matter with aerodynamic diameter less than 2.5 µm) in surface air is a severe public health concern in East Asia, but surface monitoring networks are too sparse to thoroughly assess population exposure. Satellite observations of aerosol optical depth (AOD) can provide a valuable complement (Van Donkelaar et al., 2015). Geostationary satellite sensors, including the Geostationary Ocean Color Imager (GOCI) launched by the Korea Aerospace Research Institute (KARI) in 2011 (Choi et al., 2016, 2018, 2019) and the Advanced Himawari Imager (AHI) launched by the Japanese Meteorological Agency (JMA) in 2014 (Lim et al., 2018, 2021), offer the potential for high-density mapping of PM$_{2.5}$ over East Asia (Chen et al., 2019; Wei et al., 2021a). However, more confidence is needed in relating AOD to PM$_{2.5}$. Here we evaluate the capability of the GEOS-Chem chemical transport model (CTM) to simulate AOD-PM$_{2.5}$ relationships over East Asia, exploiting in-situ aircraft measurements of vertical aerosol profiles and optical properties from the joint NASA-NIER Korea - United States Air Quality (KORUS-AQ) field study in May-June 2016 (Crawford et al., 2021; Peterson et al., 2019; Jordan et al., 2020) together with GOCI/AHI geostationary satellite data and surface measurement networks. This enables us to identify critical variables and uncertainties for inferring PM$_{2.5}$ from satellite AOD data.

69   A number of past studies have used satellite AOD data to infer surface $PM_{2.5}$ using physical and statistical models.

70   The standard geophysical approach has been to use a CTM, such as GEOS-Chem, to compute the $PM_{2.5}$/AOD ratio

71   (Liu et al., 2004; van Donkelaar et al., 2006; van Donkelaar et al., 2015; Xu et al., 2015; Geng et al., 2017), with

72   recent applications correcting for CTM biases using available $PM_{2.5}$ surface network data (Brauer et al., 2016; Van

73   Donkelaar et al., 2016; van Donkelaar et al., 2019; Hammer et al., 2020). An alternative approach is to use artificial

74   intelligence algorithms to relate satellite AOD to $PM_{2.5}$ by training on the surface network data (Hu et al., 2017;

75   Chen et al., 2018; Xiao et al., 2018; Wei et al., 2021a; Wei et al., 2021b; Pendergrass et al., 2021), and sometimes

76   including CTM values as predictors (Di et al., 2019; Xue et al., 2019). Yet another approach is to assimilate the

77   satellite-measured AODs in a CTM and correct in this manner the $PM_{2.5}$ simulation, although this requires

78   attribution of model AOD errors to specific model parameters (Kumar et al., 2019; Saide et al., 2014; Sekiyama et

79   al., 2010; Cheng et al., 2019). In all of these approaches, a better physical understanding of the AOD-$PM_{2.5}$

80   relationship as simulated by CTMs can greatly enhance the capability to infer $PM_{2.5}$ from AOD data.

81   AOD measures aerosol extinction (scattering and absorption) integrated over the atmospheric column, so that its

82   relationship to 24-hr average surface $PM_{2.5}$ (the standard air quality metric) depends on the aerosol vertical

83   distribution and optical properties, ambient relative humidity (RH), diurnal variation of $PM_{2.5}$, and contribution from

84   coarse particulate matter to AOD. Airborne measurements of aerosol vertical profiles (without species information)

85   in East Asia are limited (Zhang et al., 2006; Liu et al., 2009; Zhang et al., 2009; Sun et al., 2013; Li et al., 2017), and

86   speciated vertical profiles are rarer. AOD is highly sensitive to RH (Brock et al., 2016; Latimer and Martin et al.,

87   2019; Saide et al., 2020), but the impact from RH uncertainty on AOD simulation lacks evaluation. In addition,

88   because the AOD is a daytime measurement that needs to be related to 24-h average $PM_{2.5}$, the diurnal variation of

89    $PM_{2.5}$ needs to be understood (Guo et al., 2017; Lennartson et al., 2018). Finally, although there are studies on the

90   optical depth of coarse mode desert dust (Eck et al., 2010; Ridley et al., 2016), there has been to our knowledge no

91   study of how coarse anthropogenic PM may contribute to the AOD measurements. Coarse anthropogenic PM

92   (distinct from desert dust) is known to be high over East Asia (Chen et al., 2015; Dai et al., 2018).

93   ## 2   Data and methods

94   ### 2.1   Observations

95   We use observations over China and South Korea from multiple platforms including surface sites, aircraft, and

96   satellites (Table 1 and 2). Surface data (Table 1) include $PM_{2.5}$ from national observation networks in China (Zhai et

97   al., 2019) and South Korea (Jordan et al., 2020), speciated $PM_{2.5}$ at 7 supersites in South Korea during KORUS-AQ

98   (Choi et al., 2019), and ground-based AODs from the AERONET network at 5 sites in East China and 10 sites in

99   South Korea (21 sites during KORUS-AQ). We use total and fine-mode AODs at 500 nm wavelength from the

100   AERONET Version 3; Spectral Deconvolution Algorithm (SDA) Version 4.1 Retrieval Level 2.0 database (Giles et

101   al., 2019; O'Neill et al., 2003). The AERONET AODs at 500 nm are converted to 550 nm using total and fine mode

102   Ångström Exponents at 500 nm for consistency with the satellite AOD data.

Table 1. Surface site observations used in this work (2016)

Variable	Number of sites
PM$_{2.5}$ in East China [a]	598
PM$_{2.5}$ in South Korea [b]	130
PM$_{2.5}$ composition in South Korea (May-June 2016) [c]	7
AERONET total and fine mode AOD in East China [d]	5
AERONET total and fine mode AOD in South Korea [d]	10-21 [e]

[a] Hourly PM$_{2.5}$ from the China National Environmental Monitoring Centre (CNEMC; quotsoft.net/air/) in East China, including only sites with more than 90% data coverage in each month of 2016. Quality control of the CNEMC dataset is described in our previous study (Zhai et al., 2019). The PM$_{2.5}$ measurements are made at reference RH ≤ 35%.

[b] Hourly PM$_{2.5}$ from the AirKorea network (airkorea.or.kr), with the same data selection criteria as for East China. The PM$_{2.5}$ measurements are made at reference RH ≤ 35%.

[c] Major PM$_{2.5}$ components including sulfate, nitrate, ammonium, organic carbon, and black carbon at 7 supersites in South Korea during KORUS-AQ (May-June 2016; Choi et al., 2019). The mass concentration of organic carbon is converted to that of organic aerosol with a multiplicative factor of 1.8 based on KORUS-AQ observations (Kim et al., 2018).

[d] AODs are from the AERONET Version 3 Level 2.0 all-points database (aeronet.gsfc.nasa.gov), except that AODs at the XuZhou site in East China are from the Version 3 Level 1.5 database. AOD at 500 nm (AOD$_{500nm}$) is converted to 550 nm (AOD$_{550nm}$) using Ångström Exponent at 500 nm (AE$_{500nm}$) following: $AOD_{550nm} = AOD_{500nm}(\frac{550}{500})^{-AE_{500nm}}$.

[e] AERONET AODs in South Korea are from 10 sites for the full year of 2016 and 21 sites during KORUS-AQ.

The KORUS-AQ campaign (Table 2) includes 20 flights over the Korean peninsula and the surrounding ocean from May 2 to June 10, 2016, with vertical profiling up to 8 km altitude. We use the aircraft observations of remote and in situ aerosol extinction (scattering + absorption) coefficients, dry aerosol number size distributions, sub-micron non-refractory aerosol composition, bulk aerosol ionic composition, black carbon (BC), and relative humidity (RH).

Geostationary satellite AOD at 550 nm are retrieved by the Yonsei Aerosol Retrieval (YAER) algorithm for the GOCI (Choi et al., 2016, 2018) and AHI (Lim et al. 2018) instruments, with GOCI covering East China and South Korea and AHI covering the broad East Asia region. AOD from GOCI and AHI have a 6 km × 6 km spatial resolution and 2.5-minute (AHI) to 1-hour (GOCI) temporal resolution for 8 hours per day (09:30 to 16:30 local time). We use the fused AOD product generated from the Yonsei GOCI and AHI AOD retrievals, each using two different surface reflectance methods (Lim et al., 2021). Fusion of this four-member ensemble is done by the maximum likelihood estimate (MLE) method, with weighting and averaging based on errors determined by comparison to AERONET AOD. The fused satellite AOD product is shown by Lim et al. (2021) to have higher accuracy than its member products in comparison with AERONET data during the KORUS-AQ campaign. We will refer to it as the 'GEO satellite AOD' product in what follows.

Table 2. KORUS-AQ aircraft observations used in this work (May-June 2016).

Variable	Instrument
Aerosol extinction profile at 532 nm	HSRL [a]
Aerosol scattering coefficient at 550 nm	TSI nephelometers [b]
Aerosol absorption coefficient at 532 nm	PSAPs [c]
Aerosol dry size distribution	TSI LAS [d]
Bulk aerosol ionic composition	SAGA [e]
Sub-micron non-refractory aerosol composition	HR-ToF-AMS [f]
Black carbon concentration	HDSP2 [g]
Relative humidity	DLH [h]

[a] NASA Langley airborne High Spectral Resolution Lidar (HSRL) (Hair et al., 2008; Scarino et al., 2014).

[b] NASA Langley TSI-3563 nephelometers (Ziemba et al., 2013).

[c] Radiance Research 3-wavelength particle soot absorption photometers (PSAPs; Ziemba et al., 2013).

[d] In-situ particle size distributions over the 0.1-5.0 μm diameter range from the TSI Laser Aerosol Spectrometer (LAS) Model 3340.

[e] University of New Hampshire (UNH) Soluble Acidic Gases and Aerosol (SAGA) instrument (Dibb et al., 2003). The cutoff aerodynamic diameter of the inlet is around 4 μm, corresponding to a geometric particle diameter of 2.5 μm (McNaughton et al., 2007; McNaughton et al., 2009).

[f] University of Colorado Boulder High-Resolution Time-of-Flight Aerosol Mass Spectrometer (HR-ToF-AMS; DeCarlo et al., 2006; Nault et al., 2018; Guo et al., 2020).

[g] NOAA Humidified-Dual-Single-Particle Soot Photometer (HDSP2; Lamb et al., 2018).

[h] NASA Diode Laser Hygrometer (DLH; Podolske et al., 2003).

2.2   GEOS-Chem simulation

We use GEOS-Chem version 12.7.1 (DOI: 10.5281/zenodo.3676008) in a nested-grid simulation at a horizontal resolution of $0.5° \times 0.625°$ over East Asia (100-145 °E, 20-50 °N). GEOS-Chem simulates detailed tropospheric oxidant-aerosol chemistry and is driven here by GEOS-FP assimilated meteorological data from the NASA Global Modeling and Assimilation Office (GMAO). Boundary layer mixing uses the non-local scheme implemented by Lin and McElroy (2010). Dry deposition of gases and particles follows a standard resistance-in-series scheme (Zhang et al., 2001; Fairlie et al., 2007; Fisher et al., 2011; Jaeglé et al., 2018). Wet deposition of gases and particles includes contributions from rainout, washout, and scavenging in convective updrafts (Liu et al., 2001; Amos et al., 2012; Q. Wang et al., 2011; Q. Wang et al., 2014) with recent updates by Luo et al. (2019, 2020). We use pre-archived initial

155 conditions from Zhai et al. (2021) and run the model from December 1, 2015 to December 31, 2016. The first month

156 is used for spin-up and the year 2016 is used for analysis.

157 GEOS-Chem has been used extensively to simulate $PM_{2.5}$ and its composition in East Asia (Geng et al., 2017; Li et

158 al., 2016; Choi et al., 2019; Jeong et al., 2008; Park et al., 2021; Zhai et al., 2021). Here we use the bulk

159 representation of aerosols including sulfate (Park et al., 2004; Alexander et al., 2009), nitrate (Jaeglé et al., 2018),

160 primary and secondary organics (Pai et al., 2020), BC (Q. Wang et al., 2014), natural dust in four advected size

161 ranges (Fairlie et al., 2007), anthropogenic fine dust (Philip et al., 2017), and sea salt in two size ranges (Jaeglé et

162 al., 2011). Heterogeneous sulfate formation on aqueous aerosols is represented by a simplified parameterization

163 scheme (Y. Wang et al., 2014), where the SO_2 uptake coefficient (γ) linearly increases from 1×10^{-5} at RH ≤ 50% to

164 2×10^{-5} at RH = 100%. The thermodynamic equilibrium of sulfate-nitrate-ammonium (SNA) aerosols with the gas

165 phase is computed with ISORROPIA II (Fountoukis and Nenes, 2007; Pye et al., 2009) assuming an aqueous

166 aerosol. We include reactive uptake on dust of acid gases (HNO_3, SO_2, and H_2SO_4), limited by consumption of dust

167 alkalinity (Fairlie et al., 2010). The alkalinity of emitted dust is estimated by assuming 7.1% Ca^{2+} and 1.1% Mg^{2+} as

168 alkaline cations by dust mass (Shah et al., 2020).

169 Monthly anthropogenic emissions are from the Multi-resolution Emission Inventory in 2016 for China (MEIC;

170 Zheng et al., 2018; http://meicmodel.org) and from the KORUSv5 emission inventory at base year 2015 (Woo et al.,

171 2020; http://aisl.konkuk.ac.kr/#/emission_data/korus-aq_emissions) for other Asian countries and shipping

172 emissions. MEIC over China applies weekly and diurnal scaling factors for all anthropogenic emissions (Zheng et

173 al., 2018). The KORUSv5 agricultural NH_3 emissions apply the diurnal scaling factors from MEIC. Natural

174 emissions include NO_x from lightning (Murray et al., 2012) and soil (Hudman et al., 2012), MEGANv2 biogenic

175 volatile organic compounds (VOCs) (Guenther et al., 2012), dust (Meng et al., 2020), and sea salt (Jaeglé et al.,

176 2011). Open fire emissions are from the Global Fire Emissions Database version 4 (GFED4; van der Werf et al.,

177 2017).

178 **2.3 AOD simulation**

179 AOD in GEOS-Chem is diagnosed by integrating vertically the aerosol scattering and absorption coefficients

180 obtained with a standard Mie calculation applied to assumed size distributions, hygroscopicity, refractive indices,

181 and densities for individual aerosol components, and summing over all components (Martin et al., 2003). Optical

182 properties are listed in Table 3. Sulfate, nitrate, and ammonium share the same optical properties and are lumped as

183 an SNA aerosol component for the purpose of optical calculations. All aerosol components except dust are assumed

184 to follow log-normal size distributions. Dust includes 7 size bins (centered at radii of 0.15, 0.25, 0.4, 0.8, 1.5, 2.5,

185 and 4.0 μm) for optical calculations, with the smallest four bins partitioned by mass from the first advected dust bin

186 (< 2.5 μm in geometric diameter) following L. Zhang et al. (2013). Dust particles follow a gamma size distribution

187 within their optical size bins (Curci, 2012). The BC absorption enhancement from coating is as given by X. Wang et

188 al. (2014).

189 Our initial simulations indicated that aerosol extinction coefficients from the standard GEOS-Chem version 12.7.1

190 underestimated in situ measured extinction coefficients during KORUS-AQ by 20% on average (Figure S1). We

191 traced this problem to bias in the assumed size distributions for SNA and organic aerosol, as shown in Section 3.

192 Therefore, we re-computed the diagnostic AOD using updated log-normal size distributions for SNA and organic

193 aerosol with number median radius $R_{N,med}$ = 0.11 μm and geometric standard deviation σ = 1.4 based on KORUS-

194 AQ observations, instead of $R_{N,med}$ = 0.058 μm and σ = 1.6 in the standard model version 12.7.1, which is derived

195 from IMPROVE network measurements of aerosol mass scattering efficiency over North America (Latimer and

196 Martin, 2019).

197 **Table 3. Aerosol optical properties [a].**

Aerosol component	$R_{N,med}$, μm	σ	Hygroscopicity [b]	Refractive index	ρ, g cm^{-3}
SNA [c]	0.11	1.4	κ = 0.61	$1.53 - 6.0 \times 10^{-3}i$	1.7
Organic [c]	0.11	1.4	κ = 0.1	$1.53 - 6.0 \times 10^{-3}i$	1.3
BC	0.020	1.6	GADS	$1.75 - 4.4 \times 10^{-3}i$	1.8
Sea salt (fine)	0.085	1.5	GADS	$1.5 - 1.0 \times 10^{-3}i$	2.2
Sea salt (coarse)	0.40	1.8	GADS	$1.5 - 1.0 \times 10^{-3}i$	2.2
Dust	7 size bins	NA	κ = 0 [d]	$1.558 - 1.4 \times 10^{-3}i$	2.5-2.65 [e]

198 [a] Aerosol optical properties used in this work for computing aerosol scattering and absorption coefficients. Values
199 are from the standard GEOS-Chem model version 12.7.1, except for the size distributions of SNA and organic
200 aerosol which are based on KORUS-AQ observations (see text). All aerosol components except dust have log-
201 normal dry size distributions where $R_{N,med}$ is the number median radius and σ is the geometric standard deviation.
202 Refractive indices are for 550 nm wavelength. ρ is the dry aerosol mass density.

203 [b] Hygroscopic growth for SNA and organic aerosol as a function of relative humidity (RH, %) is computed from κ-
204 Kohler theory as a diameter growth factor GF = $(1 + \kappa * RH/(100-RH))^{1/3}$ (Latimer and Martin, 2019). Hygroscopic
205 growth factors for other aerosol components are from the Global Aerosol Data Set (GADS) as tabulated in Chin et
206 al. (2002) and Martin et al. (2003).

207 [c] $R_{N,med}$ and σ are fit to KORUS-AQ observations as described in the text. Standard GEOS-Chem v12.7.1 assumes
208 $R_{N,med}$ = 0.058 μm, σ = 1.6 (Latimer and Martin, 2019).

209 [d] Hygroscopic growth of dust particles is assumed negligible.

210 [e] Sub-micron dust particles have a density of 2.5 g cm^{-3} while coarse mode dust particles have a density of 2.65 g
211 cm^{-3}. Dust size distribution is described in the text.

3 Aerosol concentrations and optical properties during KORUS-AQ

213 Here we use the KORUS-AQ aircraft observations and their simulation with GEOS-Chem to better understand the

214 vertical distributions of different aerosol components contributing to AOD over South Korea. We begin with the

215 mean vertical profile of aerosol mass and go on to examine the aerosol optical properties. This provides the basis for

216 analyzing the observed vertical profile of aerosol extinction, its simulation by GEOS-Chem, and the consistency

217 with GEO satellite and AERONET AOD measurements over South Korea during the KORUS-AQ period.

218 **3.1 Vertical profile of aerosol mass**

219 Figure 1 shows the mean aircraft vertical profiles of aerosol mass observed during KORUS-AQ and their simulation

220 by GEOS-Chem. The KORUS-AQ aircraft sampled during the daytime, mainly between 9 am and 3 pm local time.

221 Here and elsewhere, the model is sampled along the flight tracks and at the flight times. The observed vertical

222 distribution of aerosol mass concentrations (Figure 1a) shows that 58% of column aerosol mass is below 2 km

223 altitude, which we define as the average planetary boundary layer (PBL) during KORUS-AQ, and 34% is at 2-5 km

224 altitude, which we define as the lower free troposphere (FT). The model has a similar vertical distribution (Figure

225 1b), with 57% of aerosol mass in the PBL and 36% in the lower FT. SNA, organic, and dust each contribute about a

226 third of aerosol mass in the PBL while dust dominates in the lower FT both in the observations and in the model.

227 The enhanced dust in the lower FT is driven by a few dust events, which the model reproduces (Figure S2). Black

228 carbon and sea salt (not shown) make only minor contributions to aerosol mass. The model underestimates sulfate

229 by 28% in the PBL, which leads to a 20% overestimate of nitrate, with canceling effect on the SNA mass simulation.

230 The GEOS-Chem simulation of organic aerosol in this work uses the simple scheme of Pai et al. (2020) and

231 underestimates aircraft observations by 16% in the PBL. Over 90% of GEOS-Chem organic aerosol is secondary,

232 consistent with observations (Figure S4; Nault et al., 2018; Pai et al., 2020). GEOS-Chem simulation of the

233 KORUS-AQ aerosol component profiles for different meteorological regimes is presented in Park et al. (2021).
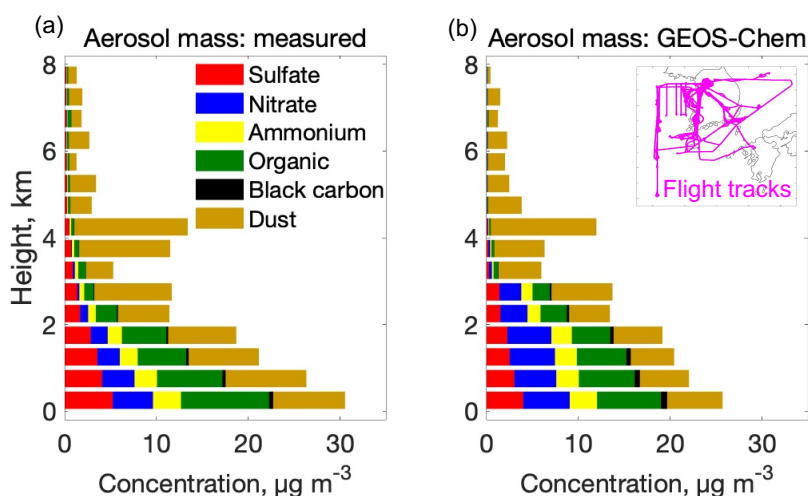
234

235 **Figure 1. Vertical profiles of aerosol mass during KORUS-AQ. Panel (a) shows the mean vertical distributions of**

236 **observed mass concentrations of major aerosol components at ambient temperature and pressure. Panel (b) is the same as**

237 **(a) but from the GEOS-Chem model sampled along the flight tracks (inset). We derive dust concentration from SAGA**

238 **Ca^{2+} and Na^+ following Shah et al. (2020) by assuming that non-sea salt Ca^{2+} accounts for 7.1% of dust mass: [dust] =**

239 **$([Ca^{2+}] – 0.0439 [Na^+]/2) / 0.071$ where the brackets denote mass concentration. Modeled dust is shown for particles with**

240 **geometric diameter < 2.5 μm, to be consistent with SAGA measurements (Table 2 footnote e). Measured sulfate, nitrate,**

241 **ammonium, and organic aerosol concentrations are from the AMS instrument (values from the SAGA instrument are**

242 **shown in Figure S4). All data are averaged over 500-m vertical bins. Here and elsewhere, we excluded pollution plumes**

243 **diagnosed by either NO_2 or SO_2 > 10 ppbv (3.4% of all the data).**

3.2   Aerosol size distributions

Figure 2a shows the normalized dry aerosol number size distributions on each of the 20 flights and in 3 altitude bands: < 1.5 km, 3-5 km, and 6-7 km (60 lines). The spread in the size distributions above 1 µm in diameter reflects dust influence. We select measurements below 1.5 km altitude when SNA + organic aerosol mass concentrations are more than 4 times that of dust as defining the SNA + organic aerosol size distributions (green lines in Figure 2a). Conditions dominated by SNA + organic aerosols define the lower envelopes of the ensemble of size distributions at diameter > 1 µm. SNA and organics were observed to have similar size distributions during KORUS-AQ (Kim et al., 2018).

Figure 2b converts the SNA + organic dominated number size distributions to volume size distributions. The observed SNA + organic dominated aerosol size distribution is shifted toward larger sizes relative to the standard GEOS-Chem. The secondary maximum in the coarse mode could be due to dust. We fitted the observed SNA + organic aerosol size distributions to a lognormal distribution with volume median radius $R_{V,med} = 0.15$ µm and geometric standard deviation $\sigma = 1.4$. The number median radius is derived from the volume median radius following Seinfeld and Pandis (2016):

$$\ln R_{N,med} = \ln R_{V,med} - 3\ln^2\sigma \tag{1}$$

which yields $R_{N,med} = 0.11$ µm. In comparison, the standard GEOS-Chem size distribution from Latimer and Martin (2019) has $R_{N,med} = 0.058$ µm and $\sigma = 1.6$. We adopt the observed log-normal size distribution parameters in what follows (Table 3).
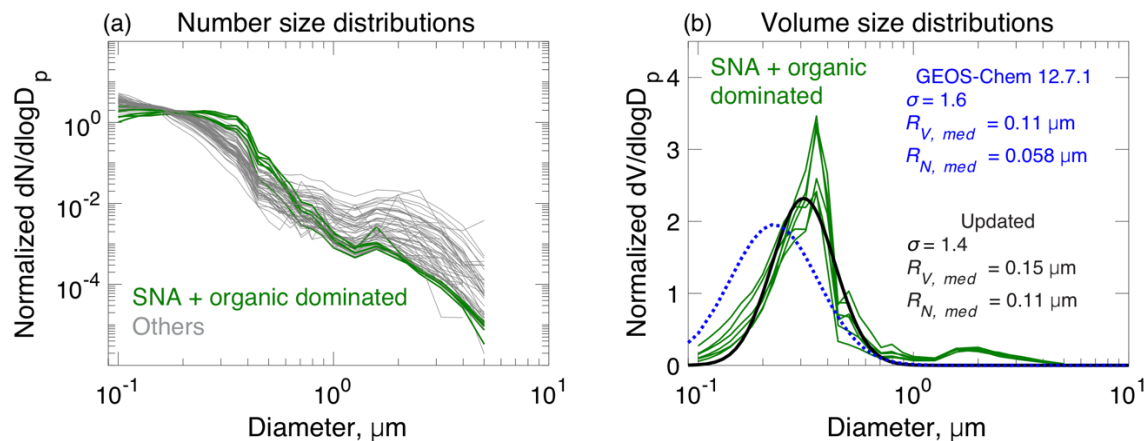
Figure 2. Aerosol dry size distributions measured in the KORUS-AQ aircraft campaign. Panel (a) shows mean normalized number size distributions measured on each of the 20 flights and for 3 altitude bins: < 1.5 km, 3-5 km, and 6-7 km (60 lines total). The SNA + organic dominated size distribution profiles are highlighted in color. Panel (b) shows normalized volume size distributions for conditions dominated by SNA + organic aerosols (green lines), along with a least-square fit to a lognormal distribution (black line), and the standard GEOS-Chem v12.7.1 size distribution from Latimer and Martin (2019) (blue dashed line). Normalization imposes an arbitrary value of unit area below each line. Lognormal distribution parameters are inset in panel (b) including volume median radius ($R_{V,med}$), number median radius ($R_{N,med}$), and geometric standard deviation (σ).

3.3 Aerosol extinction and relation to AOD

Figure 3 shows the vertical profiles of ambient aerosol extinction coefficients and RH during KORUS-AQ. Vertical profiles of aerosol extinction were measured on the aircraft both remotely with the HSRL instrument (above and below the aircraft) and in situ with TSI-3563 nephelometers (for scattering) and PSAPs (for absorption). The two agree well, as shown in Figure 3a. They indicate that 76-90% of column aerosol extinction is in the PBL at 0-2 km altitude and 9-19% is in the lower FT at 2-5 km. Both measurements show that aerosol extinction is much more strongly weighted to the PBL than aerosol mass (Figure 1).

Also shown in Figure 3a are the contributions of individual aerosol components to the extinction profile, as computed from the GEOS-Chem optical properties (Table 3) applied to the observed mass concentrations. The sum shows a good match to the measured extinction coefficient profiles. The much larger contribution of the PBL to column aerosol extinction than to column mass is because aerosol mass in the lower FT is mainly composed of dust, whose mass extinction efficiency is much smaller than SNA and organics due to its coarse size and lack of hygroscopic growth (Figure S5). The mean AOD inferred from the aircraft data is 0.36 and is contributed 59% by SNA, 27% by organic aerosol, 12% by dust, and 2% by BC. It is consistent with the mean AODs measured at AERONET stations in South Korea during KORUS-AQ (Figure S6).

Figure 3b shows the GEOS-Chem simulation of aerosol extinction profiles for comparison to the observations in Figure 3a. The model underestimates extinction coefficients by 20% below 1 km altitude, leading to a 10%

288   underestimate of aircraft inferred AOD, although there is no such underestimate in aerosol mass. This is caused by a

289   negative RH bias in the GEOS-FP meteorological data used to drive GEOS-Chem, particularly at high RH

290   conditions (Figure 3c) and is corrected if we apply the observed RH rather than the GEOS-FP RH to the GEOS-

291   Chem aerosol mass concentrations (Figure 3d).

292
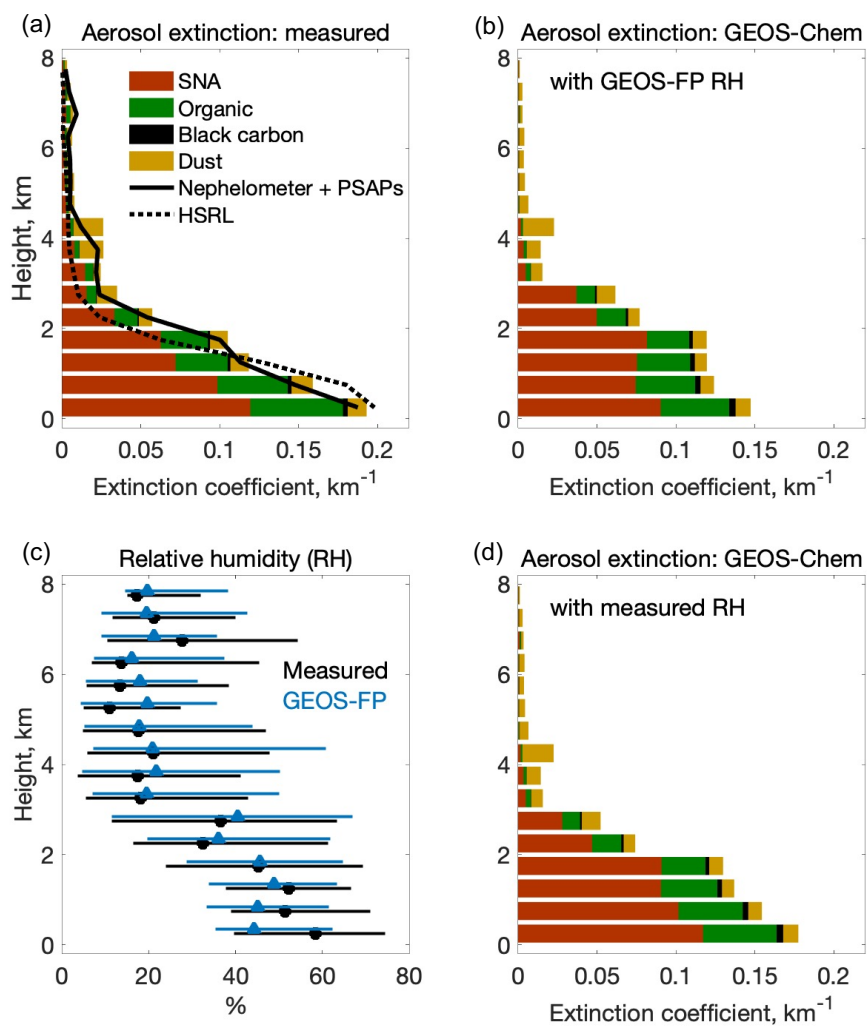
Figure 3. Vertical profiles of aerosol extinction coefficients and relative humidity (RH) during KORUS-AQ. Panel (a)

shows the mean observed vertical distributions of 550 nm extinction coefficients measured in situ (nephelometer + PSAPs;

at ambient RH) and remotely (HSRL), along with an independent calculation (colored horizontal bars) from the

measured mass concentrations of major aerosol components, measured RH, and GEOS-Chem optical properties as given

in Table 3. Panel (b) shows the mean aerosol extinction profile in GEOS-Chem and the contributions from the different

model components. Panel (c) is the median vertical profile of RH (horizontal bars are 25-75th percentiles) from aircraft

measurements and the GEOS-FP assimilated meteorological data used to drive GEOS-Chem. Panel (d) is the same as (b)

but calculated using measured RH.

301   **4   AOD and surface particulate matter over South Korea during KORUS-AQ**

302   Our analysis of Section 3 used the KORUS-AQ aircraft data together with GEOS-Chem to attribute AOD over

303   South Korea to individual aerosol components and altitudes. We now take the next step of evaluating the capability

304   of GEOS-Chem to independently simulate observed AODs and surface particulate matter concentrations.

305   Figure 4a shows the spatial distribution of the fused geostationary satellite (GOCI/AHI) AOD (GEO satellite AOD)

306   during the KORUS-AQ period with AERONET total AOD added as circles. The GEO satellite AOD shows high

307   values (0.5-0.6) along the west coast of South Korea, significantly correlated with AERONET total AOD with a

308   spatial correlation coefficient (R) of 0.7. GEO satellite AOD is biased low at sites in the Seoul Metropolitan Area

309   (SMA) and is biased high on the Yellow Sea islands, resulting in an overall -10% bias. The low biases in the SMA

310   could be due to high-concentration aerosol pixels mis-identified as clouds and/or possible issues with the aerosol

311   type assumption in the aerosol retrieval, while the high biases on the Yellow Sea islands could result from

312   uncertainties in the assumption of ocean surface reflectance, as has been discussed by Choi et al. (2016, 2018) and

313   Lim et al. (2018, 2021). Sampling the AODs at or near the seven $PM_{2.5}$ supersites operating during KORUS-AQ

314   shows no significant bias (inset values in Figure 4a).

315   Figure 4b-e shows the spatial distributions of GEOS-Chem AOD, surface PM_{10} (particulate matter with aerodynamic

316   diameter less than 10 μm), surface $PM_{2.5}$, and surface coarse PM (PM_{10} minus $PM_{2.5}$; particulate matter with

317   aerodynamic diameter less than 10 μm and larger than 2.5 μm), with surface observations shown as circles and

318   median values at the measurement sites inset. GEOS-Chem reproduces the satellite AOD enhancements along the

319   west coast of South Korea but the values are lower than observed, which we attribute to unaccounted coarse PM and

320   negative RH bias as discussed below. Comparison of AERONET total and fine mode AOD shows a 13%

321   contribution of coarse particles to total AOD. Comparison of GEOS-Chem to the fine-mode AERONET AOD, as

322   shown in Figure 4b, finds a 15% underestimate that could be attributed to the low-RH bias (Figure 3c). Concurrent

323   measurements of PM_{10} and $PM_{2.5}$ at AirKorea sites show that coarse PM (median 21 μg m^{-3}) accounts for 41% of

324   total PM_{10} (50 μg m^{-3}), while coarse PM in GEOS-Chem is much lower (3.5 μg m^{-3}; Figure 4e). Therefore, about

325   half of the GEOS-Chem underestimate of total AOD can be attributed to missing coarse PM, with the other half

326   comes from negative RH bias. Coarse PM has a concentration larger than 10 μg m^{-3} across South Korea, with higher

327   concentration in the SMA (~ 30 μg m^{-3}) than in rural areas (~ 15 μg m^{-3}), implying an origin from both

328   anthropogenic and natural sources (Figure 4e).

329   GEOS-Chem overestimates surface $PM_{2.5}$ by 43% over South Korea (Figure 4d), in contrast to the simulation of

330   AERONET fine mode AOD (Figure 4b). Figure 4f-j shows the spatial distributions of major $PM_{2.5}$ components in

331   GEOS-Chem (background) and measurements (filled circles). GEOS-Chem is not significantly biased relative to the

332   observations for organic aerosol and BC, and underestimates sulfate by 22%. We find that the model bias for $PM_{2.5}$

333   is largely driven by nitrate, which is overestimated by a factor of 3 and leads to a 56% overestimate of ammonium.

334   By contrast, comparison to the KORUS-AQ data below 1-km altitude showed only a 20% overestimate of nitrate

335   (Figure 1). This is because the model bias is mainly driven by nighttime conditions (Figure 5), while aircraft

336 samples in the daytime during KORUS-AQ. The cause of this large model bias is analyzed by K. R. Travis et al.

337 (manuscript in preparation) and is attributed to nighttime nitrate chemistry and deposition in the stratified boundary

338 layer.
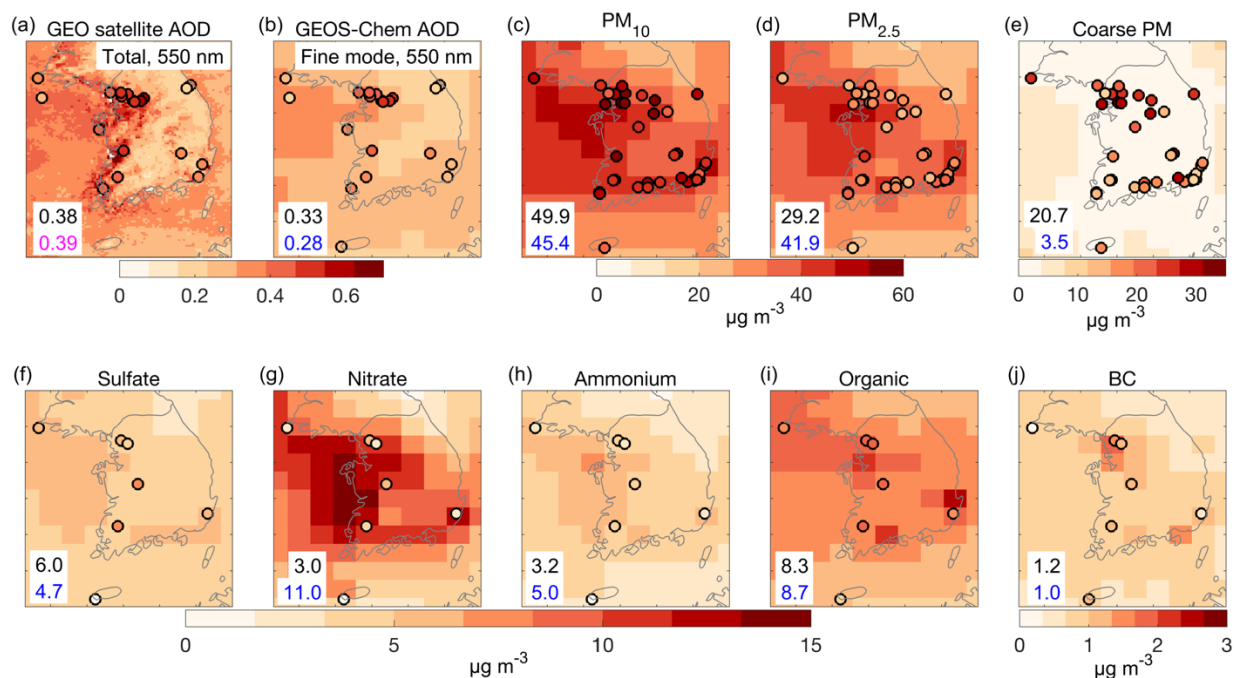
339 Ground measurements (filled circles)   Geostationary satellite (background in panel a)   GEOS-Chem (background in panels b-j)

340 **Figure 4. Spatial distributions of AOD and surface PM$_{10}$, PM$_{2.5}$, coarse PM (PM$_{10}$ minus PM$_{2.5}$), and major PM$_{2.5}$**

341 **components over South Korea averaged during KORUS-AQ (May 9 - June 10, 2016). Panel (a) shows the fused**

342 **geostationary (GEO) 550 nm AOD from the GOCI and AHI satellites (background) and AERONET 550 nm total AOD**

343 **(filled circles). Panel (b) shows GEOS-Chem 550 nm AOD sampled at hourly GEO satellite AOD (GEOS-Chem clear-sky**

344 **AOD; background) and AERONET 550 nm fine mode AOD (filled circles). Panel (c) shows surface PM$_{10}$ modelled by**

345 **GEOS-Chem (background) and measured at ground sites (filled circles). Panels (d-j) are the same as panel (c) but**

346 **respectively for PM$_{2.5}$, coarse PM (PM$_{10}$ minus PM$_{2.5}$), and sulfate, nitrate, ammonium, organic, and BC PM$_{2.5}$**

347 **components. Values inset are median values from ground-based measurements (black) and sampled from GEO satellite**

348 **(magenta) and GEOS-Chem (blue). Measured PM$_{10}$, PM$_{2.5}$, and coarse PM in panels (c-e) are shown for a random**

349 **selection of 50% of AirKorea sites to visualize spatial distribution, and inset values are for the seven supersites where**

350 **PM$_{2.5}$ composition was measured. Median AOD values inset are sampled at or near the seven supersites to avoid biasing**

351 **by the large number of sites in the Seoul Metropolitan Area. Modelled total PM$_{2.5}$ concentrations are calculated at 35%**

352 **RH (Table 3). Modelled PM$_{10}$ is the sum of PM$_{2.5}$, coarse dust, and coarse sea salt.**
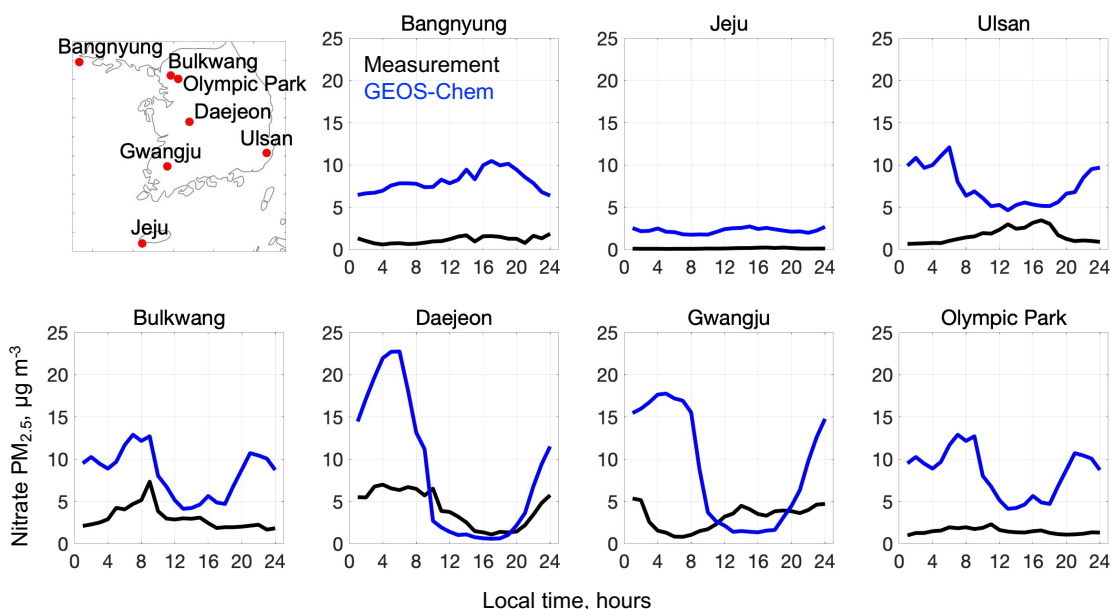
353
354 **Figure 5. Median diurnal variations of PM₂.₅ nitrate concentrations at the seven supersites (top left panel) operated in**
355 **South Korea during KORUS-AQ (May 9 - June 10, 2016). Values are medians binned by hour. GEOS-Chem model**
356 **values are sampled to coincide with the measurements.**

5 AOD and its relationship to PM₂.₅ over East Asia

358 We build on our analysis of the KORUS-AQ period for a broader interpretation of the distribution of AOD over

359 Korea and China and its relationship to surface PM₂.₅, acknowledging that the conditions sampled in KORUS-AQ

360 may not be representative of other seasons or of China. Figure 6 shows the spatial distributions of 2016 annual and

361 seasonal mean geostationary (GEO) satellite AODs, the corresponding GEOS-Chem clear-sky AODs, and GEOS-

362 Chem surface PM₂.₅. The Figure gives normalized mean biases (*NMB*s) relative to ground-based measurements from

363 AERONET and from the PM₂.₅ surface networks (shown as circles) over the North China region (115.5-122° E,

364 34.5-40.5° N) and South Korea. The North China region is defined to overlap with the domain of the geostationary

365 satellite AOD, and to ensure consistent seasonal variations within its narrow latitude.

366 On an annual mean basis, AOD over North China (~ 0.5-0.6) is about 50% larger than over South Korea (~ 0.3-0.4).

367 AOD over South Korea shows higher values (> 0.4) in the Seoul Metropolitan Area, consistent with that during the

368 KORUS-AQ period (Figure 4a). Transport from the Asian continent is strongest in spring when the frequency of

369 cold front passages is highest (Liu et al., 2003). AERONET total AOD in spring (0.4-0.6) is twice as large as fine-

370 mode AOD (0.2-0.3), reflecting a large contribution of dust. In seasons other than spring, 80-90% of AERONET

371 total AOD is contributed by the fine mode. There is large seasonality in AODs over North China, and weaker

372 seasonality over South Korea, which will be discussed below.

373 The GEOS-Chem clear-sky AODs show the same spatial and seasonal patterns as GEO satellite AODs but tend to

374 be low in spring and summer. Comparison of the model to AERONET AODs confirms this bias and shows better

375 agreement with fine-mode AOD in spring (*NMB* of -1%), implying an underestimate of coarse dust that is consistent

376 with our comparisons to the AirKorea network data (Figure 4e). Comparison of clear-sky and all-sky AODs in

377 GEOS-Chem shows no significant difference on an annual and seasonal mean basis, except for winter (Figure S7).

378 Winter has larger all-sky AOD than clear-sky AOD and the lowest rate of successful satellite retrievals (Figure S7),

379 which may be due in part to misclassification of heavy wintertime $PM_{2.5}$ pollution as clouds (Zhang et al., 2020).

380 The spatial distributions of $PM_{2.5}$ in GEOS-Chem in different seasons match closely the observations (Figure 6,

381 bottom row). We see also a close coincidence between the spatial distributions of $PM_{2.5}$ and AODs, both in the

382 observations and the model. On an annual mean basis, GEOS-Chem overestimates $PM_{2.5}$ by 16% in North China

383 and by 14% in South Korea, even though it underestimates AERONET fine mode AODs by 15%. The overestimate

384 of $PM_{2.5}$ in South Korea is worst in spring (27%), consistent with KORUS-AQ results which we previously

385 attributed to excessive nighttime nitrate build-up in the model. Over North China, the overestimate of $PM_{2.5}$ is worst

386 in summer (33%), consistent with the nitrate overestimate in summer shown in our previous study (Zhai et al.,

387 2021), which could also be due to model overestimate of nighttime nitrate (Miao et al., 2020).
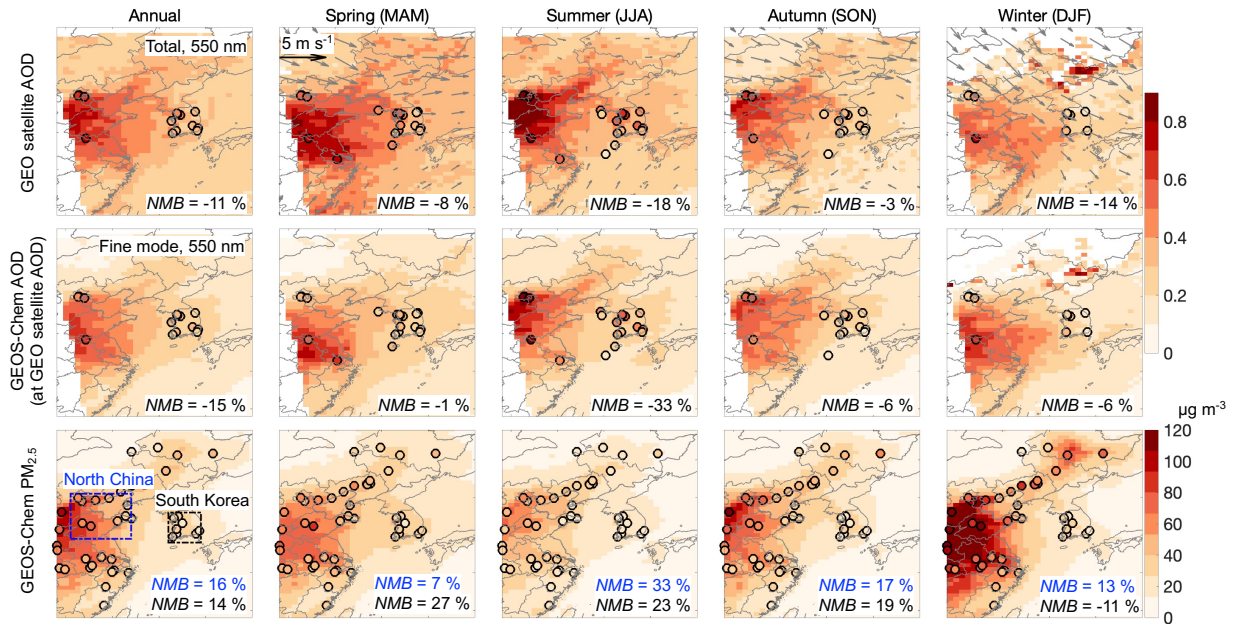
Figure 6. Spatial distributions of 2016 annual and seasonal mean AOD (550 nm) and surface PM$_{2.5}$. The top row shows the observed GOCI/AHI geostationary satellite AOD (GEO satellite AOD) on the GEOS-Chem 0.5º × 0.625º grid with superimposed 925 hPa GEOS-FP wind fields and AERONET total AODs (circles). The middle row shows clear-sky GEOS-Chem AOD, with AERONET fine mode AOD added as circles. The bottom row shows GEOS-Chem surface PM$_{2.5}$ (background) with surface network measurements (circles). AERONET AODs are shown only when more than 10 months of data are available for the annual mean and all 3 months data are available for each season. The PM$_{2.5}$ observations shown are for a random selection of 7% of network sites for visual clarity. GEOS-Chem PM$_{2.5}$ is calculated at 35% RH (Table 3). Normalized mean biases (*NMB*s) inset are for the comparisons of GEO satellite and GEOS-Chem values to the corresponding ground measurements.

Figure 7 shows daily correlations of the regional average series between AERONET total AOD and GEO satellite AOD, between AERONET fine mode AOD and GEOS-Chem AOD, as well as between measured PM$_{2.5}$ and GEOS-Chem PM$_{2.5}$. Correlations in Figure 7 are all statistically significant with correlation coefficients (*R*) ranging from around 0.7 to more than 0.9 and normalized mean biases (*NMB*) within ± 30%. The correlations of these three pairs are similar over South Korea and North China, except that GEOS-Chem overestimates springtime PM$_{2.5}$ in South Korea but not over North China, possibly due to a model overestimate of the long-range transport of PM$_{2.5}$ from China to South Korea in spring.

406
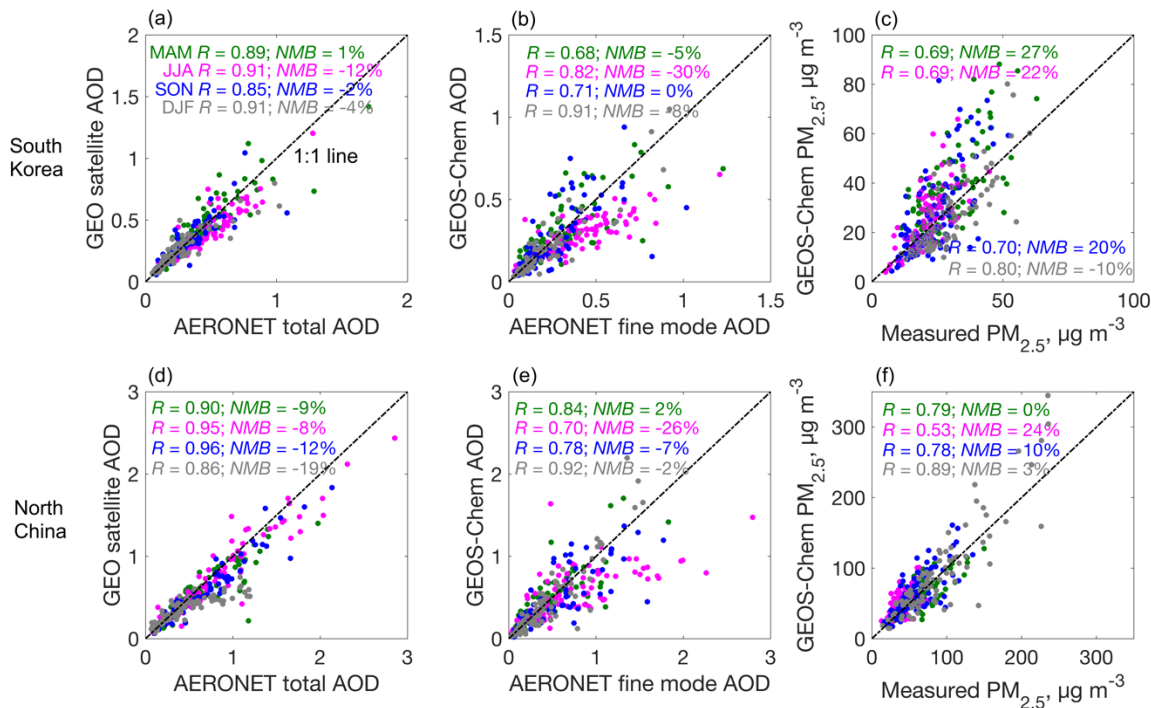
Figure 7. Scatter plots of regional mean daily (a and d) GEO satellite AOD vs. AERONET total AOD, (b and e) GEOS-Chem AOD vs. AERONET fine-model AOD, and (c and f) GEOS-Chem PM$_{2.5}$ vs. measured PM$_{2.5}$ over South Korea (a-c) and North China (d-f). Different colors represent different seasons. Values inset are correlation coefficients (*R*) and normalized mean biases (*NMB*) between surface measurements and GEO satellite or GEOS-Chem values.

411

Figure 8 compares the seasonalities of AOD and PM$_{2.5}$ over the North China and South Korea regions. The GEO satellite AOD over North China peaks in July and is minimum in winter. Most of AOD is attributed by GEOS-Chem to SNA aerosol, same as in South Korea. AOD over South Korea also has a summer maximum and winter minimum but with weaker amplitude than over North China. The GEOS-Chem AOD is ~ 20% biased low in summer and this is largely due to a low RH bias (Figure S8), as seen previously in the KORUS-AQ comparisons but amplified by the high RH in summer that drives hygroscopic growth (Latimer and Martin, 2019).

Surface PM$_{2.5}$ in the observations over North China and South Korea shows opposite seasonality to AOD, with minimum values in summer and maximum values in winter-spring. GEOS-Chem reproduces the strong seasonality of PM$_{2.5}$ in North China and the much weaker seasonality in South Korea. The high PM$_{2.5}$ values over North China in winter in the model are mostly driven by organic aerosol, reflecting the large residential coal burning source (Figure S9; Zheng et al., 2018). In South Korea, by contrast, household energy is mainly from natural gas and electricity (Lee et al., 2020; Woo et al., 2020). GEOS-FP daytime PBL height also shows a stronger seasonality over North China than over South Korea (Figure S8), generally consistent with the CALIPSO daytime PBL height (Su et al., 2018). Previous studies have shown opposite seasonality between MODIS AOD and surface PM$_{2.5}$ over North China and attributed this to the seasonality in PBL height and RH (Qu et al., 2016; Xu et al., 2019). The mean

427 PM$_{2.5}$/AOD ratio over North China in winter (236 µg m^{-3}) is 8 times that in summer (29 µg m^{-3}), with autumn (94 µg

428 m^{-3}) and spring (89 µg m^{-3}) in between, while over South Korea, the PM$_{2.5}$/AOD ratio in winter (62 µg m^{-3}) is only

429 70% larger than in summer (36 µg m^{-3}).
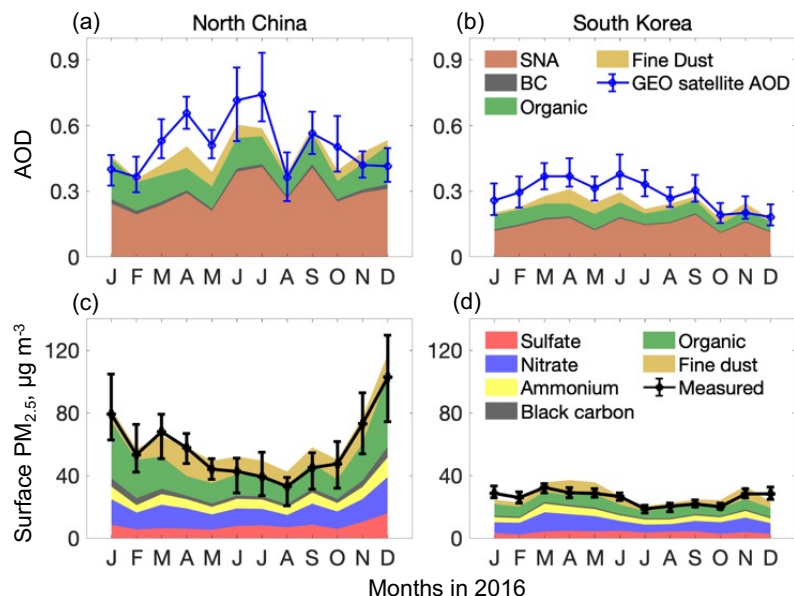
430

431 **Figure 8. Seasonality of AOD and PM$_{2.5}$ over North China and South Korea, and contributions from individual aerosol**

432 **components. Lines show regional medians (error bars: 25th and 75th percentiles) for the ensemble of monthly averaged**

433 **observations in the regions (Figure 6) in 2016. GEOS-Chem values are shown as stacked contours for individual**

434 **components and are sampled in the same way as the observations.**

435 ## 6   Conclusions

436 Geostationary satellite observations of aerosol optical depth (AOD) over East Asia may usefully complement PM$_{2.5}$

437 air quality networks if the local relationship between AOD and PM$_{2.5}$ can be inferred from a physical and/or

438 statistical model. Here we analyzed the ability of the GEOS-Chem chemical transport model to provide this

439 relationship by using a new fused GOCI/AHI geostationary satellite product together with AERONET ground-based

440 AOD measurements, aerosol vertical profiles over South Korea from the KORUS-AQ aircraft campaign (May-June

441 2016), and surface network observations. This allowed us to identify the critical features and limitations of the

442 model for successful representing the AOD-PM$_{2.5}$ relationship.

443 The KORUS-AQ observations show that total aerosol extinction (550 nm) in the vertical column is dominated by

444 sulfate-nitrate-ammonium (SNA) and organic aerosol in the planetary boundary layer (PBL), despite large

445 concentrations of dust in the free troposphere. This reflects the optically effective size and high hygroscopicity of

446 the PBL aerosols. We find that GEOS-Chem aerosol optical properties based on measurements over the North

447 America (default model setting) underestimate KORUS-AQ aerosol mass extinction efficiency by around 20%. In

448 addition, a low bias in GEOS-FP RH below 1 km leads to a 10% underestimate of AOD inferred from the aircraft

449 profile. Adjustments of GEOS-Chem aerosol optical properties and RH enable a successful simulation of the aerosol

450 extinction profile. SNA aerosol contributes 59% of column aerosol extinction in the KORUS-AQ data, while

451 organic aerosol contributes 27% and dust contributes 12%.

452 Comparison of GOCI/AHI geostationary (GEO) satellite AOD to AERONET AODs over South Korea shows good

453 agreement, with high values along the west coast. GEOS-Chem is more consistent with the fine-mode AERONET

454 AOD because of its insufficient accounting of coarse particles, which account for 13% of AERONET AOD. The

455 remaining 15% underestimate of AERONET fine-mode AOD by GEOS-Chem can be attributed to the RH low bias.

456 GEOS-Chem overestimates 24-h surface $PM_{2.5}$ over South Korea by 43% during the KORUS-AQ period, despite its

457 successful simulation of the aircraft data and fine-mode AERONET AOD, and we find that this is due to a large

458 overestimate of nighttime nitrate.

459 Broader examination of the GOCI/AHI AOD satellite data over East Asia shows spatial distributions and

460 magnitudes consistent with AERONET and featuring in particular strong Asian outflow in spring that includes a

461 large dust component. We find that AODs and $PM_{2.5}$ have similar large-scale spatial distributions but opposite

462 seasonality. $PM_{2.5}$ in North China has a strong winter maximum and summer minimum, while AOD shows the

463 opposite. GEOS-Chem simulates successfully the seasonality of measured $PM_{2.5}$ but is ~ 20% biased low in summer

464 for AOD, due again to RH low bias like that during KORUS-AQ, amplified by the high RH in summer that drives

465 hygroscopic growth (Latimer and Martin, 2019). We find that the opposite AOD and $PM_{2.5}$ seasonality is mainly

466 driven by residential coal heating sources and low PBL depths in winter, and high RH in summer. Observations of

467 $PM_{2.5}$ and AOD in South Korea show the same seasonal phases as in North China but with much weaker amplitude,

468 reflecting the lack of residential coal burning in winter and a weaker seasonal amplitude of PBL depth.

469 In summary, we find that the geostationary GOCI/AHI satellite AOD data provide high-quality information for

470 monitoring of $PM_{2.5}$ over East Asia but that physical interpretation requires accurate information on aerosol size

471 distributions, PBL depths, RH, the role of coarse particles, and diurnal variation of $PM_{2.5}$, all of which are subject to

472 large uncertainties in chemical transport models. Addressing these uncertainties should be a target of future work.

473 We have used results from our study in a recent machine-learning reconstruction of daily 2011-present $PM_{2.5}$ over

474 East Asia from GOCI AOD data by identifying critical variables for the machine-learning algorithm and providing

475 blended gap-filling data for cloudy scenes (Pendergrass et al., 2021). Besides the factors discussed in this study,

476 topography might be another important factor influencing surface $PM_{2.5}$ and its vertical mixing (Su et al., 2018), and

477 this also requires future investigation.

478

479 *Data availability.* Aircraft data during KORUS-AQ are available at: www-air.larc.nasa.gov/cgi-

480 bin/ArcView/korusaq. $PM_{2.5}$ data over China are from: quotsoft.net/air/. $PM_{2.5}$ data over South Korea are from:

481 www.airkorea.or.kr/web. AERONET data can be found at: aeronet.gsfc.nasa.gov. The MEIC emission inventory are

482 at: www.meicmodel.org/. The KORUSv5 emission inventory is developed by Konkuk University, available at:

483 http://aisl.konkuk.ac.kr/#/emission_data/korus-aq_emissions.

484

485 *Author contributions.* SZ and DJJ designed the study. SZ performed the data analysis and model simulations with

486 contributions from JFB, KL, HCL, SKK, XW, PL, KRT, and Hong Liao. JK, SL, and Hyunkwang Lim provided

487 satellite AOD data. RJP and JIJ contributed to AirKorea data processing. JM and RM provided the dust emission

488 inventory. GL, FY, and JMM updated wet deposition simulation. JWH, BEA, JED, JLJ, PCJ, and BAN contributed

489 to KORUS-AQ campaign measurements. JHW and YK provided the KORUSv5 emission inventory. QZ provided

490 the MEIC emission inventory. SZ and DJJ wrote the paper with input from all authors.

491

492 *Acknowledgement.* This work was funded by the Samsung Advanced Institute of Technology and the Harvard-

493 NUIST Joint Laboratory for Air Quality and Climate (JLAQC). JLJ, PCJ, and BAN acknowledge NASA grant

494 NNX15AT96G and 80NSSC19K0124 for support.

495

496 *Competing interests.* The authors declare that they have no conflict of interest.

497

498 **References**

499 Alexander, B., Park Rokjin, J., Jacob Daniel, J., and Gong, S.: Transition metal-catalyzed oxidation of atmospheric
500 sulfur: Global implications for the sulfur budget, J. Geophys. Res. Atmos., 114, D02309,
501 https://doi.org/10.1029/2008JD010486, 2009.

502 Amos, H. M., Jacob, D. J., Holmes, C. D., Fisher, J. A., Wang, Q., Yantosca, R. M., Corbitt, E. S., Galarneau, E.,
503 Rutter, A. P., Gustin, M. S., Steffen, A., Schauer, J. J., Graydon, J. A., Louis, V. L. S., Talbot, R. W., Edgerton, E.
504 S., Zhang, Y., and Sunderland, E. M.: Gas-particle partitioning of atmospheric Hg(II) and its effect on global
505 mercury deposition, Atmos. Chem. Phys., 12, 591-603, https://doi.org/10.5194/acp-12-591-2012, 2012.

506 Brauer, M., Freedman, G., Frostad, J., van Donkelaar, A., Martin, R. V., Dentener, F., Dingenen, R. v., Estep, K.,
507 Amini, H., Apte, J. S., Balakrishnan, K., Barregard, L., Broday, D., Feigin, V., Ghosh, S., Hopke, P. K., Knibbs, L.
508 D., Kokubo, Y., Liu, Y., Ma, S., Morawska, L., Sangrador, J. L. T., Shaddick, G., Anderson, H. R., Vos, T.,
509 Forouzanfar, M. H., Burnett, R. T., and Cohen, A.: Ambient Air Pollution Exposure Estimation for the Global
510 Burden of Disease 2013, Environ. Sci. Technol., 50, 79-88, 10.1021/acs.est.5b03709, 2016.

511 Brock, C. A., Wagner, N. L., Anderson, B. E., Beyersdorf, A., Campuzano-Jost, P., Day, D. A., Diskin, G. S.,
512 Gordon, T. D., Jimenez, J. L., Lack, D. A., Liao, J., Markovic, M. Z., Middlebrook, A. M., Perring, A. E.,
513 Richardson, M. S., Schwarz, J. P., Welti, A., Ziemba, L. D., and Murphy, D. M.: Aerosol optical properties in the
514 southeastern United States in summer – Part 2: Sensitivity of aerosol optical depth to relative humidity and aerosol
515 parameters, Atmos. Chem. Phys., 16, 5009-5019, 10.5194/acp-16-5009-2016, 2016.

516 Chen, G., Li, S., Knibbs, L. D., Hamm, N. A. S., Cao, W., Li, T., Guo, J., Ren, H., Abramson, M. J., and Guo, Y.: A
517 machine learning method to estimate $PM_{2.5}$ concentrations across China with remote sensing, meteorological and
518 land use information, Sci. Total Environ., 636, 52-60, https://doi.org/10.1016/j.scitotenv.2018.04.251, 2018.

Chen, W., Tang, H., and Zhao, H.: Diurnal, weekly and monthly spatial variations of air pollutants and air quality of Beijing, Atmos. Environ., 119, 21-34, https://doi.org/10.1016/j.atmosenv.2015.08.040, 2015.

Chen, J., Yin, J., Zang, L., Zhang, T., and Zhao, M.: Stacking machine learning model for estimating hourly $PM_{2.5}$ in China based on Himawari 8 aerosol optical depth data, Sci. Total Environ, 697, 134021, https://doi.org/10.1016/j.scitotenv.2019.134021, 2019.

Cheng, Y., Dai, T., Goto, D., Schutgens, N. A. J., Shi, G., and Nakajima, T.: Investigating the assimilation of CALIPSO global aerosol vertical observations using a four-dimensional ensemble Kalman filter, Atmos. Chem. Phys., 19, 13445-13467, https://doi.org/10.5194/acp-19-13445-2019, 2019.

Chin, M., Ginoux, P., Kinne, S., Torres, O., Holben, B. N., Duncan, B. N., Martin, R. V., Logan, J. A., Higurashi, A., and Nakajima, T.: Tropospheric Aerosol Optical Thickness from the GOCART Model and Comparisons with Satellite and Sun Photometer Measurements, J. Atmos. Sci., 59, 461-483, https://doi.org/10.1175/1520-0469(2002)059<0461:TAOTFT>2.0.CO;2, 2002.

Choi, M., Kim, J., Lee, J., Kim, M., Park, Y. J., Holben, B., Eck, T. F., Li, Z., and Song, C. H.: GOCI Yonsei aerosol retrieval version 2 products: an improved algorithm and error analysis with uncertainty estimation from 5-year validation over East Asia, Atmos. Meas. Tech., 11, 385-408, 10.5194/amt-11-385-2018, 2018.

Choi, J., Park, R. J., Lee, H.-M., Lee, S., Jo, D. S., Jeong, J. I., Henze, D. K., Woo, J.-H., Ban, S.-J., Lee, M.-D., Lim, C.-S., Park, M.-K., Shin, H. J., Cho, S., Peterson, D., and Song, C.-K.: Impacts of local vs. trans-boundary emissions from different sectors on $PM_{2.5}$ exposure in South Korea during the KORUS-AQ campaign, Atmos. Environ., 203, 196-205, https://doi.org/10.1016/j.atmosenv.2019.02.008, 2019.

Choi, M., Kim, J., Lee, J., Kim, M., Park, Y. J., Jeong, U., Kim, W., Hong, H., Holben, B., Eck, T. F., Song, C. H., Lim, J. H., and Song, C. K.: GOCI Yonsei Aerosol Retrieval (YAER) algorithm and validation during the DRAGON-NE Asia 2012 campaign, Atmos. Meas. Tech., 9, 1377-1398, https://doi.org/10.5194/amt-9-1377-2016, 2016.

Crawford, J. H., Ahn, J. Y., Al-Saadi, J., Chang, L., Emmons, L., Kim, J., Lee, G., Park, J. H., Park, R., Woo, J. H., Song, C. K., Hong, J.-H., Hong, Y.-D., Lefer, B. L., Lee, M., Lee, T., Kim, S., Min, K.-E., Yum, S. S., Shin, H. J., Kim, Y.-W., Choi, J.-S., Park, J.-S., Szykman, J. J., Long, R. W., Jordan, C. E., Simpson, I. J., Fried, A., Dibb, J. E., Cho, S. Y., and Kim, Y. P.: The Korea-United States air quality (KORUS-AQ) field study, Elementa-Sci. Anthrop., in press, 2021.

Curci, G.: FlexAOD: a chemistry-transport model post-processing tool for a flexible calculation of aerosol optical properties, 1-4, http://pumpkin.aquila.infn.it/gabri/downld/curci_istp2012.pdf, 2012.

Dai, Q., Bi, X., Liu, B., Li, L., Ding, J., Song, W., Bi, S., Schulze, B. C., Song, C., Wu, J., Zhang, Y., Feng, Y., and Hopke, P. K.: Chemical nature of $PM_{2.5}$ and PM_{10} in Xi'an, China: Insights into primary emissions and secondary particle formation, Environmental Pollution, 240, 155-166, https://doi.org/10.1016/j.envpol.2018.04.111, 2018.

Di, Q., Amini, H., Shi, L., Kloog, I., Silvern, R., Kelly, J., Sabath, M. B., Choirat, C., Koutrakis, P., Lyapustin, A., Wang, Y., Mickley, L. J., and Schwartz, J.: An ensemble-based model of $PM_{2.5}$ concentration across the contiguous United States with high spatiotemporal resolution, Environ. Int., 130, 104909, https://doi.org/10.1016/j.envint.2019.104909, 2019.

Dibb, J. E., Talbot, R. W., Scheuer, E. M., Seid, G., Avery, M. A., and Singh, H. B.: Aerosol chemical composition in Asian continental outflow during the TRACE-P campaign: Comparison with PEM-West B, J. Geophys. Res. Atmos., 108, 8815, https://doi.org/10.1029/2002JD003111, 2003.

Eck, T. F., Holben, B. N., Sinyuk, A., Pinker, R. T., Goloub, P., Chen, H., Chatenet, B., Li, Z., Singh, R. P., Tripathi, S. N., Reid, J. S., Giles, D. M., Dubovik, O., O'Neill, N. T., Smirnov, A., Wang, P., and Xia, X.: Climatological aspects of the optical properties of fine/coarse mode aerosol mixtures, J. Geophys. Res. Atmos., 115, https://doi.org/10.1029/2010JD014002, 2010.

Fairlie, T. D., Jacob, D. J., and Park, R. J.: The impact of transpacific transport of mineral dust in the United States, Atmos. Environ., 41, 1251-1266, https://doi.org/10.1016/j.atmosenv.2006.09.048, 2007.

Fairlie, T. D., Jacob, D. J., Dibb, J. E., Alexander, B., Avery, M. A., van Donkelaar, A., and Zhang, L.: Impact of mineral dust on nitrate, sulfate, and ozone in transpacific Asian pollution plumes, Atmos. Chem. Phys., 10, 3999-4012, https://doi.org/10.5194/acp-10-3999-2010, 2010.

Fisher, J. A., Jacob, D. J., Wang, Q., Bahreini, R., Carouge, C. C., Cubison, M. J., Dibb, J. E., Diehl, T., Jimenez, J. L., Leibensperger, E. M., Lu, Z., Meinders, M. B. J., Pye, H. O. T., Quinn, P. K., Sharma, S., Streets, D. G., van Donkelaar, A., and Yantosca, R. M.: Sources, distribution, and acidity of sulfate–ammonium aerosol in the Arctic in winter–spring, Atmos. Environ., 45, 7301-7318, https://doi.org/10.1016/j.atmosenv.2011.08.030, 2011.

Fountoukis, C. and Nenes, A.: ISORROPIA II: a computationally efficient thermodynamic equilibrium model for K^+–Ca^{2+}–Mg^{2+}–NH_4^+–Na^+–SO_4^{2-}–NO_3^-–Cl^-–H_2O aerosols, Atmos. Chem. Phys., 7, 4639-4659, https://doi.org/10.5194/acp-7-4639-2007, 2007.

Geng, G., Zhang, Q., Tong, D., Li, M., Zheng, Y., Wang, S., and He, K.: Chemical composition of ambient $PM_{2.5}$ over China and relationship to precursor emissions during 2005-2012, Atmos. Chem. Phys., 17, 9187–9203, https://doi.org/10.5194/acp-17-9187-2017, 2017.

Giles, D. M., Sinyuk, A., Sorokin, M. G., Schafer, J. S., Smirnov, A., Slutsker, I., Eck, T. F., Holben, B. N., Lewis, J. R., Campbell, J. R., Welton, E. J., Korkin, S. V., and Lyapustin, A. I.: Advancements in the Aerosol Robotic Network (AERONET) Version 3 database - automated near-real-time quality control algorithm with improved cloud screening for Sun photometer aerosol optical depth (AOD) measurements, Atmos. Meas. Tech., 12, 169-209, https://doi.org/10.5194/amt-12-169-2019, 2019.

Guenther, A. B., Jiang, X., Heald, C. L., Sakulyanontvittaya, T., Duhl, T., Emmons, L. K., and Wang, X.: The Model of Emissions of Gases and Aerosols from Nature version 2.1 (MEGAN2. 1): an extended and updated framework for modeling biogenic emissions, Geosci. Model Dev., 5, 1471-1492, https://doi.org/10.5194/gmd-5-1471-2012, 2012.

Guo, J., Xia, F., Zhang, Y., Liu, H., Li, J., Lou, M., He, J., Yan, Y., Wang, F., Min, M., and Zhai, P.: Impact of diurnal variability and meteorological factors on the $PM_{2.5}$ - AOD relationship: Implications for $PM_{2.5}$ remote sensing, Environ. Pollut., 221, 94-104, https://doi.org/10.1016/j.envpol.2016.11.043, 2017.

Guo, H., Campuzano-Jost, P., Nault, B. A., Day, D. A., Schroder, J. C., Dibb, J. E., Dollner, M., Weinzierl, B., and Jimenez, J. L.: The Importance of Size Ranges in Aerosol Instrument Intercomparisons: A Case Study for the ATom Mission, Atmos. Meas. Tech. Discuss., 2020, 1-49, https://doi.org/10.5194/amt-2020-224, 2020.

Hair, J. W., Hostetler, C. A., Cook, A. L., Harper, D. B., Ferrare, R. A., Mack, T. L., Welch, W., Izquierdo, L. R., and Hovis, F. E.: Airborne High Spectral Resolution Lidar for profiling aerosol optical properties, Appl. Opt., 47, 6734-6752, https://doi.org/10.1364/AO.47.006734, 2008.

Hammer, M. S., van Donkelaar, A., Li, C., Lyapustin, A., Sayer, A. M., Hsu, N. C., Levy, R. C., Garay, M., Kalashnikova, O., Kahn, R. A., Brauer, M., Apte, J. S., Henze, D. K., Zhang, L., Zhang, Q., Ford, B., Pierce, J. R., and Martin, R. V.: Global Estimates and Long-Term Trends of Fine Particulate Matter Concentrations (1998-2018), Environ. Sci. Technol., 54, 7879-7890, https://dx.doi.org/10.1021/acs.est.0c01764, 2020.

Hu, X., Belle, J. H., Meng, X., Wildani, A., Waller, L. A., Strickland, M. J., and Liu, Y.: Estimating $PM_{2.5}$ Concentrations in the Conterminous United States Using the Random Forest Approach, Environ. Sci. Technol., 51, 6936-6944, 10.1021/acs.est.7b01210, 2017.

Hudman, R. C., Moore, N. E., Mebust, A. K., Martin, R. V., Russell, A. R., Valin, L. C., and Cohen, R. C.: Steps towards a mechanistic model of global soil nitric oxide emissions: implementation and space based-constraints, Atmos. Chem. Phys., 12, 7779-7795, https://doi.org/10.5194/acp-12-7779-2012, 2012.

Jaeglé, L., Quinn, P. K., Bates, T. S., Alexander, B., and Lin, J. T.: Global distribution of sea salt aerosols: new constraints from in situ and remote sensing observations, Atmos. Chem. Phys., 11, 3137-3157, https://doi.org/10.5194/acp-11-3137-2011, 2011.

Jaeglé, L., Shah, V., Thornton, J. A., Lopez-Hilfiker, F. D., Lee, B. H., McDuffie, E. E., Fibiger, D., Brown, S. S., Veres, P., Sparks, T. L., Ebben, C. J., Wooldridge, P. J., Kenagy, H. S., Cohen, R. C., Weinheimer, A. J., Campos, T. L., Montzka, D. D., Digangi, J. P., Wolfe, G. M., Hanisco, T., Schroder, J. C., Campuzano-Jost, P., Day, D. A., Jimenez, J. L., Sullivan, A. P., Guo, H., and Weber, R. J.: Nitrogen Oxides Emissions, Chemistry, Deposition, and Export Over the Northeast United States During the WINTER Aircraft Campaign, J. Geophys. Res. Atmos., 123, 12,368-312,393, https://doi.org/10.1029/2018JD029133, 2018.

Jeong, J. I., Park, R. J., and Youn, D.: Effects of Siberian forest fires on air quality in East Asia during May 2003 and its climate implication, Atmos. Environ., 42, 8910-8922, https://doi.org/10.1016/j.atmosenv.2008.08.037, 2008.

Jordan, C. E., Crawford, J. H., Beyersdorf, A. J., Eck, T. F., Halliday, H. S., Nault, B. A., Chang, L.-S., Park, J., Park, R., and Lee, G.: Investigation of factors controlling $PM_{2.5}$ variability across the South Korean Peninsula during KORUS-AQ, Elementa-Sci. Anthrop., 8, 28, https://doi.org/10.1525/elementa.424, 2020.

Kim, H., Zhang, Q., and Heo, J.: Influence of intense secondary aerosol formation and long-range transport on aerosol chemistry and properties in the Seoul Metropolitan Area during spring time: results from KORUS-AQ, Atmos. Chem. Phys., 18, 7149-7168, https://doi.org/10.5194/acp-18-7149-2018, 2018.

Kumar, R., Delle Monache, L., Bresch, J., Saide, P. E., Tang, Y., Liu, Z., da Silva, A. M., Alessandrini, S., Pfister, G., Edwards, D., Lee, P., and Djalalova, I.: Toward Improving Short-Term Predictions of Fine Particulate Matter Over the United States Via Assimilation of Satellite Aerosol Optical Depth Retrievals, J. Geophys. Res. Atmos., 124, 2753-2773, https://doi.org/10.1029/2018JD029009, 2019.

Lamb, K. D., Perring, A. E., Samset, B., Peterson, D., Davis, S., Anderson, B. E., Beyersdorf, A., Blake, D. R., Campuzano-Jost, P., Corr, C. A., Diskin, G. S., Kondo, Y., Moteki, N., Nault, B. A., Oh, J., Park, M., Pusede, S. E., Simpson, I. J., Thornhill, K. L., Wisthaler, A., and Schwarz, J. P.: Estimating Source Region Influences on Black Carbon Abundance, Microphysics, and Radiative Effect Observed Over South Korea, J. Geophys. Res. Atmos., 123, 13,527-513,548, https://doi.org/10.1029/2018JD029257, 2018.

Latimer, R. N. C. and Martin, R. V.: Interpretation of measured aerosol mass scattering efficiency over North America using a chemical transport model, Atmos. Chem. Phys., 19, 2635-2653, https://doi.org/10.5194/acp-19-2635-2019, 2019.

Lee, W., Lim, T., and Kim, D. D.: Thermal and Energy Performance Assessment of the Prefab Electric Ondol System for Floor Heating in a Residential Building, Energies, 13, 5723, https://doi.org/10.3390/en13215723, 2020.

Lennartson, E. M., Wang, J., Gu, J., Castro Garcia, L., Ge, C., Gao, M., Choi, M., Saide, P. E., Carmichael, G. R., Kim, J., and Janz, S. J.: Diurnal variation of aerosol optical depth and $PM_{2.5}$ in South Korea: a synthesis from AERONET, satellite (GOCI), KORUS-AQ observation, and the WRF-Chem model, Atmos. Chem. Phys., 18, 15125-15144, 10.5194/acp-18-15125-2018, 2018.

Li, K., Liao, H., Zhu, J., and Moch Jonathan, M.: Implications of RCP emissions on future $PM_{2.5}$ air quality and direct radiative forcing over China, J. Geophys. Res. Atmos., 121, 12,985-913,008, https://doi.org/10.1002/2016JD025623, 2016.

Li, Z., Guo, J., Ding, A., Liao, H., Liu, J., Sun, Y., Wang, T., Xue, H., Zhang, H., and Zhu, B.: Aerosol and boundary-layer interactions and impact on air quality, Natl. Sci. Rev., 4, 810-833, 10.1093/nsr/nwx117, 2017.

Lim, H., Choi, M., Kim, J., Kasai, Y., and Chan, P.: AHI/Himawari-8 Yonsei Aerosol Retrieval (YAER): Algorithm, Validation and Merged Products, Remote Sens., 10, 699, https://doi.org/10.3390/rs10050699, 2018.

Lim, H., Go, S., Kim, J., Choi, M., Lee, S., Song, C. K., and Kasai, Y.: Integration of GOCI and AHI Yonsei aerosol optical depth products during the 2016 KORUS-AQ and 2018 EMeRGe campaigns, Atmos. Meas. Tech., 14, 4575-4592, 10.5194/amt-14-4575-2021, 2021.

Lin, J. and McElroy, M. B.: Impacts of boundary layer mixing on pollutant vertical profiles in the lower troposphere: Implications to satellite remote sensing, Atmos. Environ., 44, 1726-1739, https://doi.org/10.1016/j.atmosenv.2010.02.009, 2010.

Liu, H., Jacob, D. J., Bey, I., and Yantosca, R. M.: Constraints from ^{210}Pb and ^{7}Be on wet deposition and transport in a global three-dimensional chemical tracer model driven by assimilated meteorological fields, J. Geophys. Res. Atmos., 106, 12109-12128, https://doi.org/10.1029/2000JD900839, 2001.

Liu, H., Jacob Daniel, J., Bey, I., Yantosca Robert, M., Duncan Bryan, N., and Sachse Glen, W.: Transport pathways for Asian pollution outflow over the Pacific: Interannual and seasonal variations, J. Geophys. Res. Atmos., 108, 8786, https://doi.org/10.1029/2002JD003102, 2003.

Liu, P., Zhao, C., Liu, P., Deng, Z., Huang, M., Ma, X., and Tie, X.: Aircraft study of aerosol vertical distributions over Beijing and their optical properties, Tellus B Chem. Phys. Meteorol., 61, 756-767, 10.1111/j.1600-0889.2009.00440.x, 2009.

663 Liu, Y., Park, R. J., Jacob, D. J., Li, Q., Kilaru, V., and Sarnat, J. A.: Mapping annual mean ground-level $PM_{2.5}$
664 concentrations using Multiangle Imaging Spectroradiometer aerosol optical thickness over the contiguous United
665 States, J. Geophys. Res. Atmos., 109, D22206, https://doi.org/10.1029/2004JD005025, 2004.

666 Luo, G., Yu, F., and Moch, J. M.: Further improvement of wet process treatments in GEOS-Chem v12.6.0: impact
667 on global distributions of aerosols and aerosol precursors, Geosci. Model Dev., 13, 2879-2903,
668 https://doi.org/10.5194/gmd-13-2879-2020, 2020.

669 Luo, G., Yu, F., and Schwab, J.: Revised treatment of wet scavenging processes dramatically improves GEOS-Chem
670 12.0.0 simulations of nitric acid, nitrate, and ammonium over the United States, Geosci. Model Dev., 12, 3439-3447
671 https://doi.org/10.5194/gmd-12-3439-2019, 2019.

672 Martin, R. V., Jacob, D. J., Yantosca, R. M., Chin, M., and Ginoux, P.: Global and regional decreases in
673 tropospheric oxidants from photochemical effects of aerosols, J. Geophys. Res. Atmos., 108, 4097,
674 https://doi.org/10.1029/2002JD002622, 2003.

675 McNaughton, C. S., Clarke, A. D., Howell, S. G., Pinkerton, M., Anderson, B., Thornhill, L., Hudgins, C.,
676 Winstead, E., Dibb, J. E., Scheuer, E., and Maring, H.: Results from the DC-8 Inlet Characterization Experiment
677 (DICE): Airborne Versus Surface Sampling of Mineral Dust and Sea Salt Aerosols, Aerosol Sci. Tech., 41, 136-159,
678 https://doi.org/10.1080/02786820601118406, 2007.

679 McNaughton, C. S., Clarke, A. D., Kapustin, V., Shinozuka, Y., Howell, S. G., Anderson, B. E., Winstead, E., Dibb,
680 J., Scheuer, E., Cohen, R. C., Wooldridge, P., Perring, A., Huey, L. G., Kim, S., Jimenez, J. L., Dunlea, E. J.,
681 DeCarlo, P. F., Wennberg, P. O., Crounse, J. D., Weinheimer, A. J., and Flocke, F.: Observations of heterogeneous
682 reactions between Asian pollution and mineral dust over the Eastern North Pacific during INTEX-B, Atmos. Chem.
683 Phys., 9, 8283-8308, https://doi.org/10.5194/acp-9-8283-2009, 2009.

684 Meng, J., Martin, R. V., Ginoux, P., Hammer, M., Sulprizio, M. P., Ridley, D. A., and van Donkelaar, A.: Grid-
685 independent High Resolution Dust Emissions (v1.0) for Chemical Transport Models: Application to GEOS-Chem
686 (version 12.5.0), Geosci. Model Dev. Discuss., 1-23, https://doi.org/10.5194/gmd-2020-380, 2020.

687 Miao, R., Chen, Q., Zheng, Y., Cheng, X., Sun, Y., Palmer, P. I., Shrivastava, M., Guo, J., Zhang, Q., Liu, Y., Tan,
688 Z., Ma, X., Chen, S., Zeng, L., Lu, K., and Zhang, Y.: Model bias in simulating major chemical components of
689 $PM_{2.5}$ in China, Atmos. Chem. Phys., 20, 12265-12284, https://doi.org/10.5194/acp-20-12265-2020, 2020.

690 Murray, L. T., Jacob, D. J., Logan, J. A., Hudman, R. C., and Koshak, W. J.: Optimized regional and interannual
691 variability of lightning in a global chemical transport model constrained by LIS/OTD satellite data, J. Geophys. Res.
692 Atmos., 117, D20307, https://doi.org/10.1029/2012JD017934, 2012.

693 Nault, B. A., Campuzano-Jost, P., Day, D. A., Schroder, J. C., Anderson, B., Beyersdorf, A. J., Blake, D. R., Brune,
694 W. H., Choi, Y., Corr, C. A., de Gouw, J. A., Dibb, J., DiGangi, J. P., Diskin, G. S., Fried, A., Huey, L. G., Kim, M.
695 J., Knote, C. J., Lamb, K. D., Lee, T., Park, T., Pusede, S. E., Scheuer, E., Thornhill, K. L., Woo, J. H., and Jimenez,
696 J. L.: Secondary organic aerosol production from local emissions dominates the organic aerosol budget over Seoul,
697 South Korea, during KORUS-AQ, Atmos. Chem. Phys., 18, 17769-17800, https://doi.org/10.5194/acp-18-17769-
698 2018, 2018.

699 O'Neill, N. T., Eck, T. F., Smirnov, A., Holben, B. N., and Thulasiraman, S.: Spectral discrimination of coarse and
700 fine mode optical depth, J. Geophys. Res. Atmos., 108, https://doi.org/10.1029/2002JD002975, 2003.

701 Pai, S. J., Heald, C. L., Pierce, J. R., Farina, S. C., Marais, E. A., Jimenez, J. L., Campuzano-Jost, P., Nault, B. A.,
702 Middlebrook, A. M., Coe, H., Shilling, J. E., Bahreini, R., Dingle, J. H., and Vu, K.: An evaluation of global organic
703 aerosol schemes using airborne observations, Atmos. Chem. Phys., 20, 2637-2665, https://doi.org/10.5194/acp-20-
704 2637-2020, 2020.

705 Park, R. J., Oak, Y. J., Emmons, L. K., Kim, C.-H., Pfister, G. G., Carmichael, G. R., Saide, P. E., Cho, S.-Y., Kim,
706 S., Woo, J.-H., Crawford, J. H., Gaubert, B., Lee, H.-J., Park, S.-Y., Jo, Y.-J., Gao, M., Tang, B., Stanier, C. O.,
707 Shin, S. S., Park, H. Y., Bae, C., and Kim, E.: Multi-model intercomparisons of air quality simulations for the
708 KORUS-AQ campaign, Elementa-Sci. Anthrop., 9, 00139, https://doi.org/10.1525/elementa.2021.00139, 2021.

709 Park Rokjin, J., Jacob Daniel, J., Field Brendan, D., Yantosca Robert, M., and Chin, M.: Natural and transboundary
710 pollution influences on sulfate-nitrate-ammonium aerosols in the United States: Implications for policy, J. Geophys.
711 Res. Atmos., 109, D15204, https://doi.org/10.1029/2003JD004473, 2004.

712   Pendergrass, D. C., Jacob, D. J., Zhai, S., Kim, J., Koo, J. H., Lee, S., Bae, M., Kim, S.: Continuous mapping of fine
713   particulate matter (PM$_{2.5}$) air quality in East Asia at daily 6x6 km^2 resolution by application of a random forest
714   algorithm to 2011-2019 GOCI geostationary satellite data, submitted, 2021.

715   Peterson, D. A., Hyer, E. J., Han, S.-O., Crawford, J. H., Park, R. J., Holz, R., Kuehn, R. E., Eloranta, E., Knote, C.,
716   Jordan, C. E., and Lefer, B. L.: Meteorology influencing springtime air quality, pollution transport, and visibility in
717   Korea, Elementa-Sci. Anthrop., 7, 57, https://doi.org/10.1525/elementa.395, 2019.

718   Philip, S., Martin, R. V., Snider, G., Weagle, C. L., van Donkelaar, A., Brauer, M., Henze, D. K., Klimont, Z.,
719   Venkataraman, C., and Guttikunda, S. K.: Anthropogenic fugitive, combustion and industrial dust is a significant,
720   underrepresented fine particulate matter source in global atmospheric models, Environ. Res. Lett., 12, 044018,
721   https://doi.org/10.1088/1748-9326/aa65a4, 2017.

722   Podolske, J. R., Sachse, G. W., and Diskin, G. S.: Calibration and data retrieval algorithms for the NASA
723   Langley/Ames Diode Laser Hygrometer for the NASA Transport and Chemical Evolution Over the Pacific
724   (TRACE-P) mission, J. Geophys. Res. Atmos., 108, 8792, https://doi.org/10.1029/2002JD003156, 2003.

725   Pye, H. O. T., Liao, H., Wu, S., Mickley, L. J., Jacob, D. J., Henze, D. K., and Seinfeld, J. H.: Effect of changes in
726   climate and emissions on future sulfate-nitrate-ammonium aerosol levels in the United States, J. Geophys. Res.
727   Atmos., 114, D01205, https://doi.org/10.1029/2008JD010701, 2009.

728   Qu, W., Wang, J., Zhang, X., Sheng, L., and Wang, W.: Opposite seasonality of the aerosol optical depth and the
729   surface particulate matter concentration over the north China Plain, Atmos. Environ., 127, 90-99,
730   https://doi.org/10.1016/j.atmosenv.2015.11.061, 2016.

731   Ridley, D. A., Heald, C. L., Kok, J. F., and Zhao, C.: An observationally constrained estimate of global dust aerosol
732   optical depth, Atmos. Chem. Phys., 16, 15097-15117, 10.5194/acp-16-15097-2016, 2016.

733   Saide, P. E., Kim, J., Song, C. H., Choi, M., Cheng, Y., and Carmichael, G. R.: Assimilation of next generation
734   geostationary aerosol optical depth retrievals to improve air quality simulations, Geophys. Res. Lett., 41, 9188-9196,
735   https://doi.org/10.1002/2014GL062089, 2014.

736   Saide, P. E., Gao, M., Lu, Z., Goldberg, D. L., Streets, D. G., Woo, J. H., Beyersdorf, A., Corr, C. A., Thornhill, K.
737   L., Anderson, B., Hair, J. W., Nehrir, A. R., Diskin, G. S., Jimenez, J. L., Nault, B. A., Campuzano-Jost, P., Dibb, J.,
738   Heim, E., Lamb, K. D., Schwarz, J. P., Perring, A. E., Kim, J., Choi, M., Holben, B., Pfister, G., Hodzic, A.,
739   Carmichael, G. R., Emmons, L., and Crawford, J. H.: Understanding and improving model representation of aerosol
740   optical properties for a Chinese haze event measured during KORUS-AQ, Atmos. Chem. Phys., 20, 6455-6478,
741   https://doi.org/10.5194/acp-20-6455-2020, 2020.

742   Scarino, A. J., Obland, M. D., Fast, J. D., Burton, S. P., Ferrare, R. A., Hostetler, C. A., Berg, L. K., Lefer, B.,
743   Haman, C., Hair, J. W., Rogers, R. R., Butler, C., Cook, A. L., and Harper, D. B.: Comparison of mixed layer
744   heights from airborne high spectral resolution lidar, ground-based measurements, and the WRF-Chem model during
745   CalNex and CARES, Atmos. Chem. Phys., 14, 5547-5560, https://doi.org/10.5194/acp-14-5547-2014, 2014.

746   Sekiyama, T. T., Tanaka, T. Y., Shimizu, A., and Miyoshi, T.: Data assimilation of CALIPSO aerosol observations,
747   Atmos. Chem. Phys., 10, 39-49, https://doi.org/10.5194/acp-10-39-2010, 2010.

748   Seinfeld, J. H. and Pandis, S. N.: Atmospheric Chemistry and Physics: From Air Pollution to Climate Change, Third
749   Edition, Ch. 8, John Wiley & Sons, New Jersey, 2016.

750   Shah, V., Jacob, D. J., Moch, J. M., Wang, X., and Zhai, S.: Global modeling of cloud water acidity, precipitation
751   acidity, and acid inputs to ecosystems, Atmos. Chem. Phys., 20, 12223-12245, https://doi.org/10.5194/acp-20-
752   12223-2020, 2020.

753   Su, T., Li, Z., and Kahn, R.: Relationships between the planetary boundary layer height and surface pollutants
754   derived from lidar observations over China: regional pattern and influencing factors, Atmos. Chem. Phys., 18,
755   15921-15935, 10.5194/acp-18-15921-2018, 2018.

756   Sun, X., Yin, Y., Sun, Y., Sun, Y., Liu, W., and Han, Y.: Seasonal and vertical variations in aerosol distribution over
757   Shijiazhuang, China, Atmos. Environ., 81, 245-252, https://doi.org/10.1016/j.atmosenv.2013.08.009, 2013.

758   Travis, K. R., Crawford, J. H., Nault, B. A., Kim, H., Jordan, C. E., Chen, G., Zhai, S., Wang, X., Jimenez, J. L.,
759   Dibb, J. E., Brune, W. H., Weinheimer, A., Wennberg, P., Long, R., Szykman, J. J., Woo, J. H., Kim, Y., Li, K.,

McDuffie, E., Luo, G., Zhang, Q., Kim, S.: Why do models have difficulty simulating ammonium nitrate and nitric acid in East Asia?, manuscript in preparation.

van Donkelaar, A., Martin Randall, V., Brauer, M., and Boys Brian, L.: Use of Satellite Observations for Long-Term Exposure Assessment of Global Concentrations of Fine Particulate Matter, Environ. Health Perspect., 123, 135-143, https://doi.org/10.1289/ehp.1408646, 2015.

van Donkelaar, A., Martin, R. V., Brauer, M., Hsu, N. C., Kahn, R. A., Levy, R. C., Lyapustin, A., Sayer, A. M., and Winker, D. M.: Global Estimates of Fine Particulate Matter using a Combined Geophysical-Statistical Method with Information from Satellites, Models, and Monitors, Environ. Sci. Technol., 50, 3762-3772, https://doi.org/10.1021/acs.est.5b05833, 2016.

van der Werf, G. R., Randerson, J. T., Giglio, L., van Leeuwen, T. T., Chen, Y., Rogers, B. M., Mu, M., van Marle, M. J. E., Morton, D. C., Collatz, G. J., Yokelson, R. J., and Kasibhatla, P. S.: Global fire emissions estimates during 1997–2016, Earth Syst. Sci. Data, 9, 697-720, https://doi.org/10.5194/essd-9-697-2017, 2017.

van Donkelaar, A., Martin, R. V., Li, C., and Burnett, R. T.: Regional Estimates of Chemical Composition of Fine Particulate Matter Using a Combined Geoscience-Statistical Method with Information from Satellites, Models, and Monitors, Environ. Sci. Technol., 53, 2595-2611, 10.1021/acs.est.8b06392, 2019.

van Donkelaar, A., Martin, R. V., and Park, R. J.: Estimating ground-level PM2.5 using aerosol optical depth determined from satellite remote sensing, J. Geophys. Res. Atmos., 111, 10.1029/2005JD006996, 2006.

Wang, Q., Jacob, D. J., Fisher, J. A., Mao, J., Leibensperger, E. M., Carouge, C. C., Le Sager, P., Kondo, Y., Jimenez, J. L., Cubison, M. J., and Doherty, S. J.: Sources of carbonaceous aerosols and deposited black carbon in the Arctic in winter-spring: implications for radiative forcing, Atmos. Chem. Phys., 11, 12453-12473, https://doi.org/10.5194/acp-11-12453-2011, 2011.

Wang, Q., Jacob, D. J., Spackman, J. R., Perring, A. E., Schwarz, J. P., Moteki, N., Marais, E. A., Ge, C., Wang, J., and Barrett, S. R. H.: Global budget and radiative forcing of black carbon aerosol: Constraints from pole-to-pole (HIPPO) observations across the Pacific, J. Geophys. Res. Atmos., 119, 195-206, https://doi.org/10.1002/2013JD020824, 2014.

Wang, X., Heald, C. L., Ridley, D. A., Schwarz, J. P., Spackman, J. R., Perring, A. E., Coe, H., Liu, D., and Clarke, A. D.: Exploiting simultaneous observational constraints on mass and absorption to estimate the global direct radiative forcing of black carbon and brown carbon, Atmos. Chem. Phys., 14, 10989-11010, https://doi.org/10.5194/acp-14-10989-2014, 2014.

Wang, Y., Zhang, Q., Jiang, J., Zhou, W., Wang, B., He, K., Duan, F., Zhang, Q., Philip, S., and Xie, Y.: Enhanced sulfate formation during China's severe winter haze episode in January 2013 missing from current models, J. Geophys. Res. Atmos., 119, 10,425-410,440, https://doi.org/10.1002/2013JD021426, 2014.

Wei, J., Li, Z., Pinker, R. T., Wang, J., Sun, L., Xue, W., Li, R., and Cribb, M.: Himawari-8-derived diurnal variations in ground-level $PM_{2.5}$ pollution across China using the fast space-time Light Gradient Boosting Machine (LightGBM), Atmos. Chem. Phys., 21, 7863-7880, 10.5194/acp-21-7863-2021, 2021a.

Wei, J., Li, Z., Lyapustin, A., Sun, L., Peng, Y., Xue, W., Su, T., and Cribb, M.: Reconstructing 1-km-resolution high-quality $PM_{2.5}$ data records from 2000 to 2018 in China: spatiotemporal variations and policy implications, Remote Sens. Environ., 252, 112136, https://doi.org/10.1016/j.rse.2020.112136, 2021b.

Woo, J.-H., Kim, Y., Kim, H.-K., Choi, K.-C., Eum, J.-H., Lee, J.-B., Lim, J.-H., Kim, J., and Seong, M.: Development of the CREATE Inventory in Support of Integrated Climate and Air Quality Modeling for Asia, Sustainability, 12, 7930, https://doi.org/10.3390/su12197930, 2020.

Xiao, Q., Chang, H. H., Geng, G., and Liu, Y.: An Ensemble Machine-Learning Model To Predict Historical $PM_{2.5}$ Concentrations in China from Satellite Data, Environ. Sci. Technol., 52, 13260-13269, 10.1021/acs.est.8b02917, 2018.

Xu, J., Han, F., Li, M., Zhang, Z., Xiaohui, D., and Wei, P.: On the opposite seasonality of MODIS AOD and surface $PM_{2.5}$ over the Northern China plain, Atmos. Environ., 215, 116909, https://doi.org/10.1016/j.atmosenv.2019.116909, 2019.

807 Xu, J. W., Martin, R. V., van Donkelaar, A., Kim, J., Choi, M., Zhang, Q., Geng, G., Liu, Y., Ma, Z., Huang, L.,
808 Wang, Y., Chen, H., Che, H., Lin, P., and Lin, N.: Estimating ground-level PM2.5 in eastern China using aerosol
809 optical depth determined from the GOCI satellite instrument, Atmos. Chem. Phys., 15, 13133-13144, 10.5194/acp-
810 15-13133-2015, 2015.

811 Xue, T., Zheng, Y., Tong, D., Zheng, B., Li, X., Zhu, T., and Zhang, Q.: Spatiotemporal continuous estimates of
812 PM2.5 concentrations in China, 2000–2016: A machine learning method with inputs from satellites, chemical
813 transport model, and ground observations, Environ. Int., 123, 345-357, https://doi.org/10.1016/j.envint.2018.11.075,
814 2019.

815 Zhai, S., Jacob, D. J., Wang, X., Shen, L., Li, K., Zhang, Y., Gui, K., Zhao, T., and Liao, H.: Fine particulate matter
816 (PM$_{2.5}$) trends in China, 2013-2018: separating contributions from anthropogenic emissions and meteorology,
817 Atmos. Chem. Phys., 19, 11031-11041 https://doi.org/10.5194/acp-19-11031-2019, 2019.

818 Zhai, S., Jacob, D. J., Wang, X., Liu, Z., Wen, T., Shah, V., Li, K., Moch, J. M., Bates, K. H., Song, S., Shen, L.,
819 Zhang, Y., Luo, G., Yu, F., Sun, Y., Wang, L., Qi, M., Tao, J., Gui, K., Xu, H., Zhang, Q., Zhao, T., Wang, Y., Lee,
820 H. C., Choi, H., and Liao, H.: Control of particulate nitrate air pollution in China, Nat. Geosci.,
821 https://doi.org/10.1038/s41561-021-00726-z, 2021.

822 Zhang, L., Kok, J. F., Henze, D. K., Li, Q., and Zhao, C.: Improving simulations of fine dust surface concentrations
823 over the western United States by optimizing the particle size distribution, Geophys. Res. Lett., 40, 3270-3275,
824 https://doi.org/10.1002/grl.50591, 2013.

825 Zhang, L., Gong, S., Padro, J., and Barrie, L.: A size-segregated particle dry deposition scheme for an atmospheric
826 aerosol module, Atmos. Environ., 35, 549-560, https://doi.org/10.1016/S1352-2310(00)00326-5, 2001.

827 Zhang, Q., Zhao, C., Tie, X., Wei, Q., Huang, M., Li, G., Ying, Z., and Li, C.: Characterizations of aerosols over the
828 Beijing region: A case study of aircraft measurements, Atmos. Environ., 40, 4513-4527,
829 https://doi.org/10.1016/j.atmosenv.2006.04.032, 2006.

830 Zhang, Q., Ma, X., Tie, X., Huang, M., and Zhao, C.: Vertical distributions of aerosols under different weather
831 conditions: Analysis of in-situ aircraft measurements in Beijing, China, Atmos. Environ., 43, 5526-5535,
832 https://doi.org/10.1016/j.atmosenv.2009.05.037, 2009.

833 Zhang, X., Wang, H., Che, H.-Z., Tan, S.-C., Shi, G.-Y., and Yao, X.-P.: The impact of aerosol on MODIS cloud
834 detection and property retrieval in seriously polluted East China, Sci. Total Environ., 711, 134634,
835 https://doi.org/10.1016/j.scitotenv.2019.134634, 2020.

836 Zheng, B., Tong, D., Li, M., Liu, F., Hong, C., Geng, G., Li, H., Li, X., Peng, L., Qi, J., Yan, L., Zhang, Y., Zhao,
837 H., Zheng, Y., He, K., and Zhang, Q.: Trends in China's anthropogenic emissions since 2010 as the consequence of
838 clean air actions, Atmos. Chem. Phys., 18, 14095-14111, https://doi.org/10.5194/acp-18-14095-2018, 2018.

839 Ziemba, L. D., Lee Thornhill, K., Ferrare, R., Barrick, J., Beyersdorf, A. J., Chen, G., Crumeyrolle, S. N., Hair, J.,
840 Hostetler, C., Hudgins, C., Obland, M., Rogers, R., Scarino, A. J., Winstead, E. L., and Anderson, B. E.: Airborne
841 observations of aerosol extinction by in situ and remote-sensing techniques: Evaluation of particle hygroscopicity,
842 Geophys. Res. Lett., 40, 417-422, https://doi.org/10.1029/2012GL054428, 2013.

843